

Radius-Dependent Spin Transition of Dark Matter Halos

Jun-Sung Moon^{1,2} and Jounghun Lee¹

¹*Astronomy Program, Department of Physics and Astronomy, Seoul National University,
Seoul 08826, Republic of Korea*

jsmoon.astro@gmail.com, jounghun@astro.snu.ac.kr

²*Research Institute of Basic Sciences, Seoul National University, Seoul 08826, Republic of
Korea*

ABSTRACT

A numerical detection of the radius-dependent spin transition of dark matter halos is reported. Analyzing the data from the IllustrisTNG simulations, we measure the halo spin vectors at several inner radii within the virial boundaries and investigate their orientations in the principal frames of the tidal and velocity shear fields, called the Tweb and Vweb, respectively. The halo spin vectors in the high-mass section exhibit a transition from the Tweb intermediate to major principal axes as they are measured at more inner radii, which holds for both of the dark matter and baryonic components. The radius threshold at which the transition occurs depends on the smoothing scale, R_f , becoming larger as R_f decreases. For the case of the Vweb, the occurrence of the radius-dependent spin transition is witnessed only when $R_f \geq 1 h^{-1}$ Mpc. Repeating the same analysis but with the vorticity vectors, we reveal a critical difference from the spins. The vorticity vectors are always perpendicular to the Tweb (Vweb) major principal axes, regardless of R_f , which indicates that the halo inner spins are not strongly affected by the generation of vorticity. It is also shown that the halo spins, as well as the Tweb (Vweb) principal axes, have more directional coherence over a wide range of radial distances in the regions where the vorticity vectors have higher magnitudes. The physical interpretations and implications of our results are discussed.

Subject headings: Unified Astronomy Thesaurus concepts: Large-scale structure of the universe (902)

1. Introduction

Numerous N-body simulations have so far confirmed that the halo spin vectors tend to be intrinsically aligned with the cosmic web (see Joachimi et al. 2015; Kiessling et al. 2015, for a review). It is believed that the initial tidal interactions between the protohalos and the surrounding matter distribution originate the intrinsic spin alignments (White 1984; Lee & Pen 2000; Lee & Erdogdu 2007) and that the nonlinear processes like hierarchical merging in due subsequence should modify the alignment tendency and strength (Aragón-Calvo et al. 2007; Hahn et al. 2007; Pichon et al. 2011; Codis et al. 2012). The unique aspect of the intrinsic spin alignments of dark matter (DM) halos is that the preferred spin orientations show a transition from being parallel to being perpendicular to the hosting filaments as the halo mass increases (e.g., Aragón-Calvo et al. 2007; Hahn et al. 2007; Paz et al. 2008; Codis et al. 2012; Tempel & Libeskind 2013; Tempel et al. 2013; Trowland et al. 2013; Libeskind et al. 2013a; Aragon-Calvo & Yang 2014; Dubois et al. 2014; Forero-Romero et al. 2014; Codis et al. 2015a,b; Hirv et al. 2017; Codis et al. 2018; Ganeshiah Veena et al. 2018; Wang et al. 2018; Ganeshiah Veena et al. 2019; Kraljic et al. 2020).

This mass-dependent spin transition of DM halos was conventionally interpreted as a manifestation of the merging effect on the spin orientations (Aragón-Calvo et al. 2007; Hahn et al. 2007; Pichon et al. 2011). For the case of the high-mass halos which form through frequent merging events that preferentially occur along the filaments, their spin axes are driven to be aligned with the directions perpendicular to the filaments. Meanwhile, for the case of the low-mass halos that undergo less frequent mergers, they retain the initial tidal memory being aligned with the directions along the filaments (e.g., Codis et al. 2012; Trowland et al. 2013; Dubois et al. 2014; Codis et al. 2018; Ganeshiah Veena et al. 2018; Krolewski et al. 2019).

Another nonlinear process that can severely affect the evolution of the halo spin orientations is the generation of vorticity. In the linear regime, the peculiar velocity field is curl-free and proportional to the gradient of the perturbation potential. As it evolves, however, the nonlinearly evolved velocity field develops a curl mode, i.e., the vorticity (Pichon & Bernardeau 1999; Pueblas & Scoccimarro 2009; Kitaura et al. 2012) on a small scale, which can affect the halo angular momentum, amplifying its magnitude and reorienting its direction. Showing by N-body simulations that the vorticity vectors measured at the halo positions exhibit a strong alignment with the halo spins, Libeskind et al. (2013b) claimed that the generation of vorticity in the nonlinear regime is largely responsible for the occurrence of the spin transition phenomenon as well as for the intrinsic spin alignments of DM halos with the cosmic web in the nonlinear regime (see also Libeskind et al. 2014, and references therein).

In this picture, it is naturally expected that the variation of the tendencies and strengths of the intrinsic spin alignments with radial distance, say, *the spin alignment profile*, should be a good indicator of the evolutionary processes that the halos experience. At inner radii, it may reflect the nonlinear effects including violent relaxation and generation of vorticity, while at outer radii, it should contain the memory of the latest mergers and infalls along the cosmic web. Complementing the mass density profile of DM halos that is most commonly used to describe the halo internal structure (Navarro, Frenk & White 1996), the spin alignment profiles of DM halos may be useful to understand their merging history and internal dynamics and to relate them with the cosmic web.

Besides, what can be observed from real galaxies is the stellar spin axes that are usually measured at inner radii much smaller than the virial boundaries (Romanowsky et al. 2003; Emsellem et al. 2007; Coccato et al. 2009; Cortese et al. 2016; Welker et al. 2020). For a proper test of any theoretical predictions against observations, it is urged to find the halo spin alignment profile which can link theoretically predictable spin vectors at virial boundaries with observationally measurable spin directions at inner radii. In our prior work of Lee et al. (2021), it was found from high-resolution hydrodynamical simulations that the stellar spin vectors of massive galactic halos exhibit a *peculiar* tendency of being aligned with the directions of maximum matter compression, to which the DM spin vectors are always perpendicular, even though the stellar and DM spin vectors exhibit fairly strong alignments with each other. It was originally suspected that non-gravitational baryonic feedbacks after merging events might be responsible for this peculiar tidal connection of the galaxy stellar spin axes (Lee et al. 2021, 2022). In the follow-up works, however, it was revealed that the peculiar alignment tendency of the stellar spin vectors is likely to be established during the quiescent period when no merging events disturb the galactic halos (Lee & Moon 2022).

A key difference, however, existed between the DM and stellar components in the way that their spin directions are measured with respect to the cosmic web. While the former was measured at the halo virial boundary as usual, twice the stellar half-mass radius, $2r_{1/2\star}$, was used for the measurements of the latter, given the observational limitations (Romanowsky et al. 2003; Emsellem et al. 2007; Coccato et al. 2009; Cortese et al. 2016; Welker et al. 2020). The consequential issues regarding the halo spin alignment profile are the followings. First, will the DM spin axes of the halos, if measured at $2r_{1/2\star}$, also exhibit similar peculiar alignments with the directions of maximum matter compression? Second, is the type of the halo spin transition dependent on the radii at which the spin vectors are measured? If so, what will be the transition radius threshold? Third, does the generation of vorticity have anything to do with the peculiar alignments of the stellar spin vectors?

In this paper, we will address all of these issues by analyzing the high-resolution N-

body and hydrodynamical simulations. For a more comprehensive analysis, we will use two different web-identification algorithms, since the tendency and strength of the intrinsic spin alignments of the DM halos are known to depend on how to define the cosmic web (e.g., Forero-Romero et al. 2014). The upcoming sections contain the following contents. In Section 2, the simulation data are briefly described, and the numerical analysis is fully laid out. In Section 3, the results of the analysis and our physical interpretations of them are presented. In Section 4, a concise summary of the main results is provided, and a final conclusion is drawn. Throughout this paper, we will assume a flat universe whose energy densities are dominantly contributed by the cosmological constant Λ and cold DM at the present epoch.

2. Data and Numerical Analysis

The data on which our analysis is based are from two cosmological simulations: a DM-only N-body simulation called the TNG300-1-Dark and a hydrodynamic simulation called the TNG300-1, both of which were performed on a periodic box of volume $250 h^{-3} \text{Mpc}^3$ for a Planck ΛCDM cosmology (Planck Collaboration et al. 2016), appertaining to a suite of the IllustrisTNG project (Marinacci et al. 2018; Naiman et al. 2018; Nelson et al. 2018; Pillepich et al. 2018; Springel et al. 2018; Nelson et al. 2019). The TNG300-1-Dark simulation contains only 2500^3 DM particles of mass resolution $m_d = 7.0 \times 10^7 M_\odot$, while the TNG300-1 simulation contains not only DM particles of resolution $m_d = 5.9 \times 10^7 M_\odot$ but also an equal number of baryonic gas cells of initial resolution $m_b = 1.1 \times 10^7 M_\odot$, whose evolution was tracked by the Arepo code (Springel 2010) that is capable of incorporating the essential hydrodynamical processes. We refer the readers to the IllustrisTNG web page¹ for full information on the simulations.

The halo catalogs from each of the two simulations contain the bound groups and their substructures identified by the friends-of-friends (FoF) and Subfind algorithms (Springel et al. 2001), respectively. From here on, we will refer to the substructures of the FoF groups as the halos. We first investigate how many particles each halo from the TNG300-1-Dark simulation at $z = 0$ has within a certain radius, R_s , from the center. The value of R_s is chosen to be smaller than the virial boundary of each halo, r_{vir} , within which the spherically averaged mass density exceeds 200 times the critical density. Then, we select only those halos consisting of more than 300 DM particles within R_s to calculate the angular momentum vector

¹<https://www.tng-project.org/data/>

at an inner radius, $\mathbf{J}(R_s)$:

$$\mathbf{J}(R_s) = \sum_{\alpha=1}^{n_d} m_d [(\mathbf{x}_{d,\alpha} - \mathbf{x}_c) \times (\mathbf{v}_{d,\alpha} - \mathbf{v}_c)], \quad (1)$$

where n_d is the number of DM particles within R_s , $\mathbf{x}_{d,\alpha} = (x_{d,\alpha i})$ and $\mathbf{v}_{d,\alpha} = (v_{d,\alpha i})$ are the comoving position and peculiar velocity of the α th DM particle within R_s , respectively, while $\mathbf{x}_c = (x_{c,i})$ and $\mathbf{v}_c = (v_{c,i})$ are the positions and velocities of the halo center, respectively. We exclude those halos with $n_d \leq 300$ on the ground that the presence of shot noise would significantly contaminate the calculation of $\mathbf{J}(R_s)$ if $n_d \leq 300$ (Bett et al. 2007). Hereafter, the unit angular momentum vector, $\mathbf{j}_d(R_s) \equiv \mathbf{J}(R_s)/|\mathbf{J}(R_s)|$, will be called the halo inner (virial) spin vector if $R_s < r_{\text{vir}}$ ($R_s = r_{\text{vir}}$).

For each halo from the TNG300-1 simulations, we calculate the inner spin vectors of the DM, non-stellar gas, and stellar components separately, denoted by $\mathbf{j}_d(R_s)$, $\mathbf{j}_g(R_s)$, and $\mathbf{j}_s(R_s)$, respectively, in a very similar manner. Given that for real galaxies it is usually possible to measure their stellar spin vectors only within $2r_{1/2\star}$ due to the observational limitation (Romanowsky et al. 2003; Emsellem et al. 2007; Coccato et al. 2009; Cortese et al. 2016; Welker et al. 2020), we compute $\mathbf{j}_d(R_s)$, $\mathbf{j}_g(R_s)$ and $\mathbf{j}_s(R_s)$ at two different inner radii, $R_s = r_{1/2\star}$ and $R_s = 2r_{1/2\star}$. It is worth mentioning here that we apply the particle number cut, 300, separately to each component. For example, for the computation of $\mathbf{j}_s(R_s)$, we select only those halos consisting of more than 300 *stellar* particles.

From the full snapshot data of the two simulations at $z = 0$ released by the IllustrisTNG project, we construct three different fields: the tidal, velocity shear, and vorticity fields smoothed by a Gaussian kernel with a filtering radius of R_f on the 512^3 grid points. For the case of the TNG300-1 simulation, all of the DM, non-stellar gas, and stellar particles are used to construct these three fields, while for the other case only the DM particles are used. For the construction of the tidal fields, we follow the same procedure² as described in Lee et al. (2021) and Lee et al. (2022). We first construct the real-space density contrast field, $\delta(\mathbf{x})$, out of the spatial distributions of all particles with the help of the cloud-in-cell method and then carry out a Fourier transformation of it, $\delta(\mathbf{k})$, to compute the Gaussian filtered Fourier-space tidal field, $\mathbf{T}(\mathbf{k}) = [T_{ij}(\mathbf{k})]$ with $T_{ij}(\mathbf{k}) = [k_i k_j \delta(\mathbf{k})/|\mathbf{k}|^2] \exp(-|\mathbf{k}|^2 R_f^2/2)$. Finally, we construct the real-space tidal field, $\mathbf{T}(\mathbf{x}) = [T_{ij}(\mathbf{x})]$, through an inverse Fourier transformation and find their three eigenvalues and corresponding orthonormal eigenvectors, $\mathbf{e}_t = (e_{ti})$, through the similarity transformation at the grids where the selected halos are located. The directions of maximum (minimum) matter compression at the halo positions

²In the previous works of Lee et al. (2021) and Lee et al. (2022), the tidal fields are reconstructed from the spatial distributions of DM halos. In the current work, it is from the particle snapshot.

are often regarded as being parallel to \mathbf{e}_{t1} (\mathbf{e}_{t3}) corresponding to the largest (smallest) eigenvalue of \mathbf{T} . Meanwhile, the linear tidal torque theory predicts initial alignments of the halo spin orientations with \mathbf{e}_{t2} . Hereafter, the orientations of the cosmic web defined by the axes of \mathbf{e}_{t1} , \mathbf{e}_{t2} , and \mathbf{e}_{t3} will be referred to as *the Tweb major, intermediate, and minor principal axes*, as in Forero-Romero et al. (2014), respectively.

Taking the exactly same prescription given by Libeskind et al. (2013a) and Libeskind et al. (2014), we also construct the velocity shear $\Sigma = (\Sigma_{ij})$ and vorticity fields $\mathbf{w} = (w_i)$ by separating the deformation tensor field into a symmetric and an anti-symmetric term. Applying the cloud-in-cell method to the comoving peculiar velocities of all particles, we first calculate the mean peculiar velocity field, $\mathbf{v}(\mathbf{x}) = (v_i)$, on the 512^3 grids. Then, we find a Fourier space velocity field, $\mathbf{v}(\mathbf{k})$, to obtain a Gaussian filtered Fourier-space deformation tensor field, $\xi_{ij}(\mathbf{k})$, as $\xi_{ij}(\mathbf{k}) \equiv \iota k_j v_i(\mathbf{k}) \exp(-|\mathbf{k}|^2 R_f^2/2)$, where ι is the imaginary unit. As prescribed in Libeskind et al. (2014), we express $\xi_{ij}(\mathbf{k})$ as a sum of its symmetric and anti-symmetric terms, $\Sigma = (\Sigma_{ij})$ and $\Gamma = (\Gamma_{ij})$, respectively,

$$\xi_{ij}(\mathbf{k}) = H(z) [-\Sigma_{ij}(\mathbf{k}) + \Gamma_{ij}(\mathbf{k})] \quad (2)$$

$$\equiv \frac{1}{2} [\iota k_j v_i(\mathbf{k}) + \iota k_i v_j(\mathbf{k})] e^{-|\mathbf{k}|^2 R_f^2/2} + \frac{1}{2} [\iota k_j v_i(\mathbf{k}) - \iota k_i v_j(\mathbf{k})] e^{-|\mathbf{k}|^2 R_f^2/2}, \quad (3)$$

where $H(z)$ is the Hubble constant at a given redshift z . The Fourier-space vorticity field, $\mathbf{w}(\mathbf{k})$ is then determined from the anti-symmetric tensor, $\Gamma_{ij}(\mathbf{k})$, as $w_i = -\epsilon_{ijk} \Gamma_{jk} H(z)$ where ϵ_{ijk} is the anti-symmetric Levi-Civita symbol. The inverse Fourier transformations of $\Sigma(\mathbf{k})$ and $\mathbf{w}(\mathbf{k})$ finally lead us to obtain the real-space Gaussian filtered velocity shear and vorticity fields, $\Sigma(\mathbf{x})$ and $\mathbf{w}(\mathbf{x})$, respectively. The orthonormal eigenvectors of $\Sigma(\mathbf{x})$ at the halo positions are also found via the similarity transformation and denoted by \mathbf{e}_{v1} , \mathbf{e}_{v2} , and \mathbf{e}_{v3} corresponding to the largest, second largest, and smallest eigenvalues, respectively. The cosmic web whose orientations are parallel to $\{\mathbf{e}_{v1}, \mathbf{e}_{v2}, \mathbf{e}_{v3}\}$ is called the Vweb (e.g., Libeskind et al. 2013a; Forero-Romero et al. 2014). The left (middle) panel of Figure 1 plots the four types of the cosmic web, namely, knots, filaments, sheets, and voids identified by the signs of the Tweb (Vweb) eigenvalues (Hahn et al. 2007) on the scale of $1 h^{-1}$ Mpc, while its right panel depicts the magnitudes of the vorticity vectors on the same scale. These plots are all made in the two dimensional space projected onto the Cartesian z -axis from the TNG300-1-Dark simulation.

To investigate the radius dependence of the halo spin alignments with the cosmic web from the TNG300-1-Dark simulation, we basically calculate the following quantities as a function of halo total mass, M_h (i.e., the sum of the masses of all member particles) whose range is split into small bins,

$$\{\langle |\mathbf{j}_d(R_s) \cdot \mathbf{e}_{ti}(R_f)| \rangle, \langle |\mathbf{j}_d(R_s) \cdot \mathbf{e}_{vi}(R_f)| \rangle | i \in \{1, 2, 3\}, R_s \in \{r_{\text{vir}}, r_{\text{vir}}/2, r_{\text{vir}}/4, r_{\text{vir}}/8\} \}, \quad (4)$$

for three different cases of the smoothing scale of $R_f/(h^{-1}\text{Mpc}) \in \{0.5, 1, 2\}$. Here, the ensemble average is taken over the halos whose masses fall in the same mass bin. The associated errors are also calculated as one standard deviations in the mean values at each mass bin. The halo inner spins, $\mathbf{j}_d(R_s)$, will be described as being preferentially aligned with the i th principal axis of the Tweb on the scale of R_f if the following conditions are satisfied: (i) The ensemble average, $\langle |\mathbf{j}_d(R_s) \cdot \mathbf{e}_i(R_f)| \rangle$, is higher than 0.5 with statistical significance. (ii) It is also higher than $\langle |\mathbf{j}_d(R_s) \cdot \mathbf{e}_j(R_f)| \rangle$ and $\langle |\mathbf{j}_d(R_s) \cdot \mathbf{e}_k(R_f)| \rangle$ with statistical significance where $j \neq i$ and $k \neq i$. These criteria will be consistently used to test the existence of the alignments of the other vectors throughout this paper.

To explore how the alignment tendency of the halo inner spins differs among the DM, gas and stellar components from the TNG300-1 simulations, we also separately calculate

$$\{ \langle |\mathbf{j}_d(R_s) \cdot \mathbf{e}_{ti}(R_f)| \rangle, \langle |\mathbf{j}_d(R_s) \cdot \mathbf{e}_{vi}(R_f)| \rangle | i \in \{1, 2, 3\}, R_s \in \{r_{1/2\star}, 2r_{1/2\star}\} \}, \quad (5)$$

$$\{ \langle |\mathbf{j}_g(R_s) \cdot \mathbf{e}_{ti}(R_f)| \rangle, \langle |\mathbf{j}_g(R_s) \cdot \mathbf{e}_{vi}(R_f)| \rangle | i \in \{1, 2, 3\}, R_s \in \{r_{1/2\star}, 2r_{1/2\star}\} \}, \quad (6)$$

$$\{ \langle |\mathbf{j}_s(R_s) \cdot \mathbf{e}_{ti}(R_f)| \rangle, \langle |\mathbf{j}_s(R_s) \cdot \mathbf{e}_{vi}(R_f)| \rangle | i \in \{1, 2, 3\}, R_s \in \{r_{1/2\star}, 2r_{1/2\star}\} \}, \quad (7)$$

for the same three cases of R_f . To see how the vorticity vectors are aligned with the halo inner spins from the TNG300-1-Dark simulation, we calculate

$$\{ \langle |\mathbf{j}_d(R_s) \cdot \mathbf{w}(R_w)| \rangle | R_s \in \{r_{\text{vir}}, r_{\text{vir}}/2, r_{\text{vir}}/4, r_{\text{vir}}/8\}, R_w \in \{4r_{\text{vir}}\} \}. \quad (8)$$

Here $\mathbf{w}(R_w)$ represents the vorticity vectors at each mass bin smoothed on a scale of $R_w = 4r_{\text{vir}}$ with corresponding mean virial radii r_{vir} . Unlike the tidal and velocity shear fields that are smoothed on a fixed scale of R_f , the vorticity field is smoothed on a varying scale, given that the vorticity effect on the halos with mass M_h is known to rapidly fade away on the scales beyond four times the corresponding virial radii r_{vir} (Libeskind et al. 2013a,b, 2014).

To investigate how the presence of baryons affects the spin-vorticity alignments, we calculate

$$\{ \langle |\mathbf{j}_d(R_s) \cdot \mathbf{w}(R_w)| \rangle | R_s \in \{r_{1/2\star}, 2r_{1/2\star}\}, R_w \in \{4r_{\text{vir}}\}, \}, \quad (9)$$

$$\{ \langle |\mathbf{j}_g(R_s) \cdot \mathbf{w}(R_w)| \rangle | R_s \in \{r_{1/2\star}, 2r_{1/2\star}\}, R_w \in \{4r_{\text{vir}}\}, \}, \quad (10)$$

$$\{ \langle |\mathbf{j}_s(R_s) \cdot \mathbf{w}(R_w)| \rangle | R_s \in \{r_{1/2\star}, 2r_{1/2\star}\}, R_w \in \{4r_{\text{vir}}\}, \}, \quad (11)$$

from the TNG300-1 simulations. To see if the vorticity vectors also exhibit a similar alignment in the principal frame of the Tweb (Vweb) even at inner radii to the spin vectors, we also calculate

$$\{ \langle |\mathbf{w}(4r_{\text{vir}}) \cdot \mathbf{e}_{ti}(R_f)| \rangle, \langle |\mathbf{w}(4r_{\text{vir}}) \cdot \mathbf{e}_{vi}(R_f)| \rangle | i \in \{1, 2, 3\}, R_f/(h^{-1}\text{Mpc}) \in \{0.5, 1, 2\} \}, \quad (12)$$

from both of the TNG300-1-Dark and TNG300-1 simulations.

To explore the effect of vorticity on the strengths of the alignments between the halo inner and virial spins from the TNG300-1-Dark simulation, we also divide the selected halos into four subsamples according to their values of $\mathbf{j}_d(r_{\text{vir}}) \cdot \mathbf{j}_d(r_{\text{vir}}/8)$ and control them to share the identical mass and density joint distributions. We take the ensemble average of $\log |\mathbf{w}|/H_0$ over each of the controlled samples. If $\langle \log |\mathbf{w}|/H_0 \rangle$ turns out to significantly differ among the four subsamples, then it can be attributed not to the differences in M_h and δ but only to the difference in $\mathbf{j}_d(r_{\text{vir}}) \cdot \mathbf{j}_d(r_{\text{vir}}/8)$. In other words, it would confirm the existence of the net vorticity effect on the alignment strengths of the halo spins at different radii from the TNG300-1-Dark. The alignments between the small-scale Tweb and the large-scale Vweb major principal axes, $|\mathbf{e}_{t1}(R_f = 0.5 h^{-1} \text{Mpc}) \cdot \mathbf{e}_{v1}(R_f = 2 h^{-1} \text{Mpc})|$, are also used to create another set of four controlled subsamples and then to investigate if and how $\langle \log |\mathbf{w}|/H_0 \rangle$ varies among them. We also repeat the same calculations but from the TNG300-1 simulation to see if the presence of baryons affects the relation between the vorticity magnitude and the spin alignments, if any.

3. Results and Physical Interpretations

3.1. Inner Spin Alignments with the Cosmic Web

Figure 2 shows how the mass variations of the alignment tendencies between the halo inner spins and the Tweb principal axes depend on the radial distances, R_s , for the case of $R_f = 2 h^{-1} \text{Mpc}$, from the TNG300-1-Dark simulation at $z = 0$. As can be seen, at $R_s = r_{\text{vir}}$, we reproduce the well known mass-dependent spin transition phenomenon: the preferred directions of the halo virial spins transit from the Tweb intermediate to minor principal axes as the halo mass decreases below a threshold³ around $M_h \approx 10^{12} h^{-1} M_\odot$ (e.g., Aragón-Calvo et al. 2007; Hahn et al. 2007; Codis et al. 2012; Tempel & Libeskind 2013; Aragón-Calvo & Yang 2014; Forero-Romero et al. 2014; Codis et al. 2018; Lee et al. 2021). This type of spin transition was dubbed the type II spin transition by Lee et al. (2021) in their attempt to differentiate it from the type I spin transition between \mathbf{e}_{t1} and \mathbf{e}_{t3} exhibited by the stellar spin vectors. Note also that the halo virial spins seem to be perpendicular to the Tweb major principal axes over almost the entire mass range, which is consistent with

³Lee et al. (2020) proposed a very refined rigorous way to determine the threshold mass at which the spin transition occurs based on the Kolmogorov–Smirnov test. In the current analysis, however, we do not adopt this rigorous method because it is not the main focus of our work to accurately determine the transition threshold. Rather, we use the simple conventional criterion mentioned in Section 2.

the results of the previous works (Libeskind et al. 2014; Forero-Romero et al. 2014; Lee et al. 2021).

At inner radii $R_s < r_{\text{vir}}$, however, we witness quite different phenomena. At $R_s = r_{\text{vir}}/2$, the inner spins of the massive halos with $M_h \gtrsim 10^{13} h^{-1} M_\odot$ are still strongly aligned with the Tweb intermediate principal axes. Although the strength of the $\mathbf{j}_d\text{-}\mathbf{e}_{t2}$ alignment decreases as the halo mass decreases similar to the case of $R_s = r_{\text{vir}}$, no significant signal of the mass-dependent type II spin transition is found for this case. At $R_s = r_{\text{vir}}/4$, the inner spins of the halos with $M_h \gtrsim 10^{13} h^{-1} M_\odot$ exhibit the *peculiar* alignments with the Tweb major principal axes, being random with respect to the intermediate and perpendicular to the minor principal axes. In spite of the rapid decrease of the $\mathbf{j}_d\text{-}\mathbf{e}_{t1}$ alignment strength with the decrement of M_h , no significant signal of the occurrence of the mass-dependent halo spin transition is found. At $R_s = r_{\text{vir}}/8$, the alignments of the halo inner spins with the Tweb major principal axes are witnessed in the larger mass range of $M_h \gtrsim 10^{12} h^{-1} M_\odot$. These results clearly demonstrate that the halo spin transition occurs not only in a mass-dependent way but also in a radius-dependent way and that the radius threshold for the spin transition between \mathbf{e}_{t2} and \mathbf{e}_{t1} is not universal but dependent upon the halo virial radii. The lower mass limit, M_{th} , above which the $\mathbf{j}_d(R_s)\text{-}\mathbf{e}_{t1}$ alignment tendency is found becomes smaller as the ratio R_s/r_{vir} decreases. In other words, the alignments between the halo inner spins and the Tweb major principal axes can be found even in the lower mass section if the inner spins are measured at more inner radii.

Figure 3 plots the same as Figure 2 but with the Tweb smoothed on a smaller scale of $R_f = 1 h^{-1} \text{Mpc}$. As can be seen, for this case the transition of \mathbf{j}_d from \mathbf{e}_{t2} to \mathbf{e}_{t1} occurs at more outer radii than for the case of $R_f = 2 h^{-1} \text{Mpc}$. Even at $R_s = r_{\text{vir}}/2$, a substantial signal of the $\mathbf{j}_d\text{-}\mathbf{e}_{t1}$ alignment tendency is found in the highest mass bin with $M_h \gtrsim 10^{14} h^{-1} M_\odot$. Figure 4 plots the same as Figure 2 but on the scale of $R_f = 0.5 h^{-1} \text{Mpc}$. As can be seen, even the halo *virial spins* in the highest mass section with $M_h \gtrsim 10^{14} h^{-1} M_\odot$ appear to be aligned with the Tweb major principal axes. Note also that on this small scale the value of M_{th} rapidly decreases from $10^{13} h^{-1} M_\odot$ to $10^{11} h^{-1} M_\odot$ as R_s/r_{vir} decreases from 1/2 to 1/8.

The halos from the TNG300-1 simulation turn out to yield similar results. Figures 5–6 show the same as Figures 2–4 but from the TNG300-1 with the inner spins of the DM (top panel), non-stellar gas (middle panel) and stellar components (bottom panel) measured separately at two innermost radii $R_s = 2r_{1/2\star}$ and $r_{1/2\star}$. Note that the peculiar spin alignments with the Tweb major principal axes are found not only from the stellar components but also from the other two counterparts and that the $\mathbf{j}_d\text{-}\mathbf{e}_{t1}$ and $\mathbf{j}_s\text{-}\mathbf{e}_{t1}$ alignments are more similar to each other in their tendencies than the $\mathbf{j}_g\text{-}\mathbf{e}_{t1}$ counterpart. These results imply that the mechanism responsible for the peculiar spin alignment should affect not only the baryonic

particles but also the DM counterparts, in contrast to what Lee et al. (2021) speculated in their original work. A notable difference, however, exists between the DM and stellar components in their spin alignments measured at the innermost radii. The occurrence of the type I spin transition is witnessed from the latter but not from the former, for all the cases of R_f and R_s .

Figures 7–11 plot the same as Figures 2–6 but with the Vweb substituting for the Tweb. As can be seen, for the cases of the larger smoothing scales, $R_f = 2 h^{-1}$ Mpc and $1 h^{-1}$ Mpc, the results from the Vweb are very similar to those from the Tweb. However, a sharp difference is found for the case of the smaller smoothing scale, $R_f = 0.5 h^{-1}$ Mpc, where no significant signal of the $\mathbf{j}_d\text{--}\mathbf{e}_{t1}$ alignment is found, in direct contrast to the results from the Tweb. In fact, for this case, both of the halo inner and virial spins show no significant signal of the alignments with the Vweb principal axes. Given the well known finding that the Vweb significantly deviates from the Tweb on the nonlinear scales where the velocity field develops a strong curl mode (Libeskind et al. 2014), one may suspect that the generation of vorticity must be related to this difference between the Tweb and the Vweb on the scale of $R_f = 0.5 h^{-1}$ Mpc. In the following subsection, we explore the net effect of vorticity on the alignment strengths and tendencies of the halo spin vectors with the cosmic web.

3.2. Vorticity Effect

Figures 12–13 show how the vorticity vectors are aligned with the Tweb and Vweb principal axes, respectively, as a function of M_h for the three different cases of R_f from the TNG300-1-Dark simulation. As can be seen, the vorticity vectors exhibit the type II transition at some threshold mass whose value appears to increase with R_f for both of the Tweb and Vweb cases, which are very similar to the spin case. Nevertheless, we find a marked difference in the alignment and transition tendency between the spin and vorticity orientations in the Tweb and Vweb principal frames. Not to mention that the overall strengths of the alignments of the vorticity vectors with the Tweb and Vweb principal axes are higher, no significant signal of the type I and type II transition is exhibited by the vorticity vectors even on the scale of $0.5 h^{-1}$ Mpc. Regardless of the values of R_f and M_h , the vorticity vectors seem to be aligned with the directions perpendicular to the Tweb and Vweb major principal axes, although the alignment strength tends to decrease as M_h increases. The existence of this difference implies that the halo inner spins are rather unattached to the nonlinear modification caused by the generation of vorticity, which the halo virial spins experience.

Figure 14 shows how strongly the vorticity vectors are aligned with the halo virial and

inner spins. We do not take the absolute values of the alignment angles for this case, since the directions of the two vectors are measurable, unlike the Tweb and Vweb principal axes. The top panel plots the $\mathbf{j}_d\text{-}\mathbf{w}$ alignments measured at four different radii from the TNG300-1-Dark simulation. The halo spin vectors measured at $R_s = r_{\text{vir}}$ yield a significant tendency of being aligned with the vorticity vectors in the high-mass section, consistent with the previous findings (Libeskind et al. 2013b). However, the strength of the $\mathbf{j}_d\text{-}\mathbf{w}$ alignment rapidly decreases as M_h decreases and as R_s becomes lower than r_{vir} . The bottom panel plots the $\mathbf{j}_d\text{-}\mathbf{w}$, $\mathbf{j}_g\text{-}\mathbf{w}$, and $\mathbf{j}_s\text{-}\mathbf{w}$ alignments measured at $2r_{1/2\star}$ as a function of M_h from the TNG300-1 simulation. As can be seen, none of the three spin vectors measured at $2r_{1/2\star}$ exhibit a strong alignment with the vorticity vectors, which supports the scenario that the halo inner spins are not susceptible to the vorticity effect.

Figure 15 plots the mean magnitudes of the logarithms of the rescaled vorticity vectors, $\log |\mathbf{w}|/H_0$ (top panel), mean density contrasts in the logarithmic scale (middle panel) and mean halo mass (bottom panel) averaged over each of the four controlled subsamples of the halos classified by the values of $\mathbf{j}_d(r_{\text{vir}}) \cdot \mathbf{j}_d(r_{\text{vir}}/8)$ from the TNG300-1-Dark simulation. Note first that the four subsamples are indeed well controlled enough to have almost identical mean mass and density contrasts to one another. It guarantees that any difference in the vorticity magnitudes, if found, among the four subsamples should be attributed to the differences not in the halo mass nor in the local densities but in the strengths of the alignments between the spin vectors measured at the two different radii, r_{vir} and $r_{\text{vir}}/8$. As can be seen, there is a clear signal of the variation of $\langle \log |\mathbf{w}|/H_0 \rangle$ with the subsamples. The more strongly the inner and virial spins are aligned with each other, the higher magnitudes the vorticity vectors have. Figure 16 plots the same as Figure 15 but with the subsamples classified by $\mathbf{j}_d(r_{1/2\star}) \cdot \mathbf{j}_s(r_{1/2\star})$ from the TNG300-1 simulation, which exhibits a similar trend. The vorticity vectors tend to have higher magnitudes when the DM and stellar spin vectors at $r_{1/2\star}$ are more strongly aligned with each other. The results shown in Figures 15–16 indicate that in the regions with high vortical motions the halo spin vectors tend to have more coherent directions across radii, regardless of the components.

Figures 17–18 plot the same as Figures 15–16 but with the subsamples classified by $|\mathbf{e}_{t1}(0.5 h^{-1} \text{ Mpc}) \cdot \mathbf{e}_{v1}(2 h^{-1} \text{ Mpc})|$ from the TNG300-1-Dark and TNG300-1 simulations, respectively. As can be seen, the higher vorticity magnitudes are found in the subsamples of the halos located in the regions where the large-scale Vweb and small-scale Tweb are more strongly aligned with each other. Note the consistency of this result with that shown in Figures 15–16. The weaker alignments between $\mathbf{e}_{t1}(0.5 h^{-1} \text{ Mpc})$ and $\mathbf{e}_{v1}(2 h^{-1} \text{ Mpc})$ can be translated into the weaker alignments between $\mathbf{j}_d(r_{\text{vir}})$ and $\mathbf{j}_d(r_{\text{vir}}/8)$, since the latter tends to be aligned with the major principal axes of the small-scale Tweb in the wide mass range while the halo virial spins are aligned with the directions perpendicular to the major principal

axes of the large-scale Vweb in the whole mass range considered.

4. Summary and Discussion

We have explored how the halo spin vectors change their preferred directions with respect to the cosmic web if they are measured at inner radii smaller than the virial boundaries by analyzing the data from the DM-only and hydrodynamical simulations of the IllustrisTNG project (Marinacci et al. 2018; Naiman et al. 2018; Nelson et al. 2018; Pillepich et al. 2018; Springel et al. 2018; Nelson et al. 2019). Given that the velocity fields develop vortical motions in the nonlinear regime (Pichon & Bernardeau 1999; Kitaura et al. 2012; Libeskind et al. 2013a; Hahn et al. 2015), we have also investigated if and how the generation of vorticity affects the alignment tendency and strength between the halo inner spins and the cosmic web. Using two different algorithms, called the Tweb and Vweb finders (Libeskind et al. 2014; Forero-Romero et al. 2014), to identify the cosmic web, we have also tested their validity and efficiency in capturing the variation of the alignment tendency of the halo inner spins with radial distances.

Our findings are summarized as follows:

- The halos in a certain mass range from the TNG300-1-Dark simulations exhibit a radius-dependent spin transition in the principal frame of the Tweb for all of the three different cases of $R_f/(h^{-1} \text{Mpc}) = 0.5, 1$ and 2 . The preferred directions of their spin vectors measured at inner radii smaller than their virial boundaries, $R_s < r_{\text{vir}}$, transit from the Tweb intermediate to major principal axes where the ratio, R_s/r_{vir} , is reduced down to some threshold, u_{th} . Meanwhile, in the Vweb principal frame, a similar radius-dependent spin transition is witnessed only for the case of $R_f \geq 1 h^{-1} \text{Mpc}$.
- The radius ratio threshold, u_{th} , sensitively depends on R_f , as well as on the halo mass M_h . For the case of $R_f \geq 1 h^{-1} \text{Mpc}$, the occurrence of the radius-dependent transition is witnessed in the large mass range of $M_h \geq 10^{12} h^{-1} M_\odot$. The more massive the halos are, the larger value u_{th} has. For the case $R_f = 0.5 h^{-1} \text{Mpc}$, however, the massive halos with $M_h \gtrsim 10^{13} h^{-1} M_\odot$ show alignments with the Tweb *major* principal axes even at $u_{\text{th}} = 1$, which implies that the alignments between the halo inner spins and the Tweb major principal axes occur in the mass bin with corresponding inner radii greater than R_f .
- The inner spins of the halo DM components measured at $r_{1/2\star}$ and $2r_{1/2\star}$ from the TNG300-1 simulations exhibit the same peculiar alignments with the Tweb major

principal axes as those of the halo non-stellar gas and stellar components. However, the occurrence of the mass-dependent type I spin transition between the Tweb major and minor principal axes is witnessed only from the gas and stellar spin vectors but not from the DM counterparts.

- Unlike the halo spins, the vorticity vectors show no significant tendency of being aligned with the Tweb major principal axes, regardless of M_h and R_f . But, it has a net effect of enhancing the alignments between the halo inner and virial spins, the alignments between the DM and stellar spins measured at $r_{1/2\star}$, and the alignments between the major principal axes of the small-scale Tweb and large-scale Vweb.

Three key implications of our results are the following. First, although the vorticity developed in the nonlinear regime may originate the halo virial spins as claimed by Libeskind et al. (2013b), it must have little effect on the directions of the halo inner spins given the obvious difference in their alignment tendencies with the Tweb major principal axes. Second, unlike what Lee et al. (2021) originally speculated, the peculiar alignment tendency of the halo stellar spins at $2r_{1/2\star}$ with the Tweb major principal axes should not be ascribed to any baryonic effects. Rather, the alignments of the stellar vectors at $2r_{1/2\star}$ with the Tweb *minor* principal axes are likely to be enhanced by some non-gravitational baryonic effects, given that the DM spins at $2r_{1/2\star}$ show no alignments with the Tweb minor principal axes even in the lowest mass section. Some baryonic process like galactic winds that can discharge stellar materials from the low-mass halos might occur anisotropically along the directions of filaments, which eventually lead the stellar spins at $2r_{1/2\star}$ to acquire a tendency of being aligned with the Tweb minor principal axes (e.g., Tenneti et al. 2017). Third, on the small scale of $R_f \simeq 0.5 h^{-1}$ Mpc, the Tweb principal frame is more efficient in capturing the peculiar alignments of the halo inner spins than the Vweb counterpart.

We speculate that the peculiar alignments of the halo inner spins with the Tweb major principal axes may be a fossil record of the gravitational process that the halo progenitors undergo at early epochs when the velocity field has yet to develop full vortical flows. Recall the result of Lee & Moon (2022) that the stellar spin vectors at $2r_{1/2\star}$ are more strongly aligned with the Tweb major principal axes if the halos experience the latest merger events at earlier times. During the quiescent time without experiencing any merger, the interior of a halo can retain the tendency of its spin being aligned with the Tweb major principal axes. The merging events along the nonlinear cosmic web may stir up the interior particles of halos and drive them to have spins aligned with the directions perpendicular to the Tweb major principal axes, creating coherence in the spin directions across inner radii.

Recall also what Vera-Ciro et al. (2011) discovered by analyzing the Milky-way size galactic halos from a high-resolution simulation about the halo shape profiles. The halo

shapes measured at different radii turned out to reflect well their progenitor history, gradually switching from being prolate to being oblate as the radial distances increase from the innermost regions out to the virial boundaries. Vera-Ciro et al. (2011) explained that the differences in the merging directions along the cosmic web between the past and present epochs must be the origin of this radius-dependent shape transitions of galactic halos. We claim here that our results can also be explained by a similar logic. When the matter becomes compressed first along the Tweb major principal axes at early epochs where no vortical motions are yet to be generated, it creates peculiar spin alignments. In the subsequent evolutions, when the second and third collapse proceeds at later epochs where the velocity field begins to develop a curl mode, the halo virial spins acquire an opposite tendency of being perpendicular to the Tweb major principal axes, while the inner spins still retain the memory of the earlier merging history.

We believe that the halo spin alignment profile contains more information on the history of merging events along the cosmic web than the halo shape profile since the former is determined not only by the spatial distributions of particles but also by their velocities unlike the latter. To concrete this scenario and to test it against real observations, however, a much more comprehensive numerical analysis must be done by tracking down the directions of infalling DM materials at all different epochs, which is beyond the scope of this paper. We intend to pursue a follow-up work in this direction, hoping to report the results elsewhere in the near future.

We thank an anonymous referee for useful comments which helped us improve the original manuscript. The IllustrisTNG simulations were undertaken with compute time awarded by the Gauss Centre for Supercomputing (GCS) under GCS Large-Scale Projects GCS-ILLU and GCS-DWAR on the GCS share of the supercomputer Hazel Hen at the High Performance Computing Center Stuttgart (HLRS), as well as on the machines of the Max Planck Computing and Data Facility (MPCDF) in Garching, Germany. JSM acknowledges the support by the NRF of Korea grant funded by the Korean government (MEST) (No. 2019R1A6A1A10073437). JL acknowledges the support by Basic Science Research Program through the National Research Foundation (NRF) of Korea funded by the Ministry of Education (No.2019R1A2C1083855).

REFERENCES

- Aragón-Calvo, M. A., van de Weygaert, R., Jones, B. J. T., et al. 2007, *ApJ*, 655, L5.
- Aragon-Calvo, M. A., & Yang, L. F. 2014, *MNRAS*, 440, L46
- Bett, P., Eke, V., Frenk, C. S., et al. 2007, *MNRAS*, 376, 21
- Coccatto, L., Gerhard, O., Arnaboldi, M., et al. 2009, *MNRAS*, 394, 1249
- Codis, S., Pichon, C., Devriendt, J., et al. 2012, *MNRAS*, 427, 3320
- Codis, S., Gavazzi, R., Dubois, Y., et al. 2015, *MNRAS*, 448, 3391
- Codis, S., Pichon, C., & Pogosyan, D. 2015, *MNRAS*, 452, 3369
- Codis, S., Jindal, A., Chisari, N. E., et al. 2018, *MNRAS*, 481, 4753
- Cortese, L., Fogarty, L. M. R., Bekki, K., et al. 2016, *MNRAS*, 463, 170
- Dubois, Y., Pichon, C., Welker, C., et al. 2014, *MNRAS*, 444, 1453
- Emsellem, E., Cappellari, M., Krajnović, D., et al. 2007, *MNRAS*, 379, 401
- Forero-Romero, J. E., Contreras, S., & Padilla, N. 2014, *MNRAS*, 443, 1090
- Ganeshaiyah Veena, P., Cautun, M., van de Weygaert, R., et al. 2018, *MNRAS*, 481, 414
- Ganeshaiyah Veena, P., Cautun, M., Tempel, E., et al. 2019, *MNRAS*, 487, 1607
- González, R. E., Prieto, J., Padilla, N., et al. 2017, *MNRAS*, 464, 4666
- Hahn, O., Carollo, C. M., Porciani, C., et al. 2007, *MNRAS*, 381, 41
- Hahn, O., Teyssier, R., & Carollo, C. M. 2010, *MNRAS*, 405, 274
- Hahn, O., Angulo, R. E., & Abel, T. 2015, *MNRAS*, 454, 3920.
- Hirv, A., Pelt, J., Saar, E., et al. 2017, *A&A*, 599, A31
- Joachimi, B., Cacciato, M., Kitching, T. D., et al. 2015, *Space Sci. Rev.*, 193, 1.
- Kiessling, A., Cacciato, M., Joachimi, B., et al. 2015, *Space Sci. Rev.*, 193, 67.
- Kitaura, F.-S., Angulo, R. E., Hoffman, Y., et al. 2012, *MNRAS*, 425, 2422.
- Kraljic, K., Davé, R., & Pichon, C. 2020, *MNRAS*, 493, 362

- Krolewski, A., Ho, S., Chen, Y.-C., et al. 2019, *ApJ*, 876, 52
- Laigle, C., Pichon, C., Codis, S., et al. 2015, *MNRAS*, 446, 2744
- Lee, J. & Pen, U.-L. 2000, *ApJ*, 532, L5.
- Lee, J. & Pen, U.-L. 2001, *ApJ*, 555, 106.
- Lee, J. & Erdogdu, P. 2007, *ApJ*, 671, 1248
- Lee, J., Libeskind, N. I., & Ryu, S. 2020, *ApJ*, 898, L27
- Lee, J., Moon, J.-S., Ryu, S., et al. 2021, *ApJ*, 922, 6.
- Lee, J., Moon, J.-S., & Yoon, S.-J. 2022, *ApJ*, 927, 29.
- Lee, J. & Moon, J.-S. 2022, *ApJ*, 936, 119.
- Libeskind, N. I., Hoffman, Y., Forero-Romero, J., et al. 2013, *MNRAS*, 428, 2489
- Libeskind, N. I., Hoffman, Y., Steinmetz, M., et al. 2013, *ApJ*, 766, L15
- Libeskind, N. I., Hoffman, Y., & Gottlöber, S. 2014, *MNRAS*, 441, 1974
- Marinacci, F., Vogelsberger, M., Pakmor, R., et al. 2018, *MNRAS*, 480, 5113
- Naiman, J. P., Pillepich, A., Springel, V., et al. 2018, *MNRAS*, 477, 1206
- Navarro, J. F., Frenk, C. S., & White, S. D. M. 1996, *ApJ*, 462, 563
- Nelson, D., Pillepich, A., Springel, V., et al. 2018, *MNRAS*, 475, 624
- Nelson, D., Springel, V., Pillepich, A., et al. 2019, *Computational Astrophysics and Cosmology*, 6, 2
- Paz, D. J., Stasyszyn, F., & Padilla, N. D. 2008, *MNRAS*, 389, 1127
- Pichon, C. & Bernardeau, F. 1999, *A&A*, 343, 663
- Pichon, C., Pogosyan, D., Kimm, T., et al. 2011, *MNRAS*, 418, 2493
- Pillepich, A., Nelson, D., Hernquist, L., et al. 2018, *MNRAS*, 475, 648
- Planck Collaboration, Ade, P. A. R., Aghanim, N., et al. 2016, *A&A*, 594, A1
- Pueblas, S. & Scoccimarro, R. 2009, *Phys. Rev. D*, 80, 043504

- Romanowsky, A. J., Douglas, N. G., Arnaboldi, M., et al. 2003, *Science*, 301, 1696
- Shi, J., Wang, H., & Mo, H. J. 2015, *ApJ*, 807, 37
- Springel, V., White, S. D. M., Tormen, G., et al. 2001, *MNRAS*, 328, 726
- Springel, V., Pakmor, R., Pillepich, A., et al. 2018, *MNRAS*, 475, 676
- Springel, V. 2010, *ARA&A*, 48, 391. doi:10.1146/annurev-astro-081309-130914
- Tempel, E., & Libeskind, N. I. 2013, *ApJ*, 775, L42
- Tempel, E., Stoica, R. S., & Saar, E. 2013, *MNRAS*, 428, 1827
- Tenneti, A., Gnedin, N. Y., & Feng, Y. 2017, *ApJ*, 834, 169
- Trowland, H. E., Lewis, G. F., & Bland-Hawthorn, J. 2013, *ApJ*, 762, 72
- Vera-Ciro, C. A., Sales, L. V., Helmi, A., et al. 2011, *MNRAS*, 416, 1377
- Wang, X., Szalay, A., Aragón-Calvo, M. A., et al. 2014, *ApJ*, 793, 58
- Wang, P., Guo, Q., Kang, X., et al. 2018, *ApJ*, 866, 138
- Welker, C., Bland-Hawthorn, J., Van de Sande, J., et al. 2020, *MNRAS*, 491, 2864
- White, S. D. M. 1984, *ApJ*, 286, 38
- Zhu, W. & Feng, L.-L. 2017, *ApJ*, 838, 21

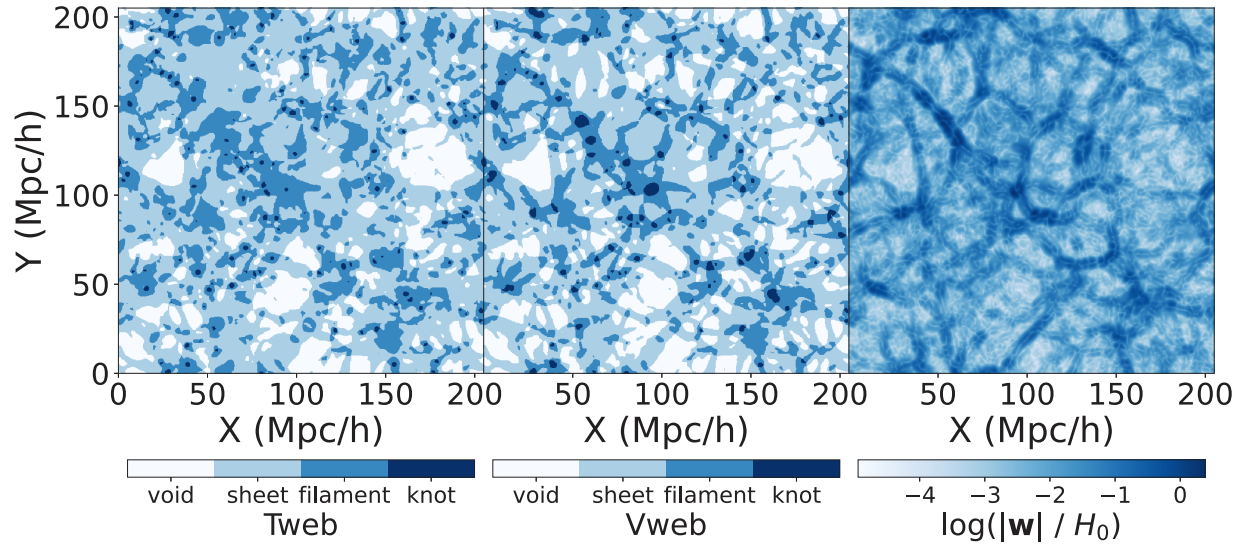


Fig. 1.— Four types of the cosmic web identified by the eigenvalue signs of the Tweb (left panel) and Vweb (middle panel) smoothed on the scale of $R_f = 1 h^{-1} \text{Mpc}$, and the magnitudes of the vorticity field (right panel) in the two dimensional space projected onto the Cartesian z -axis from the TNG300-1-Dark simulation.

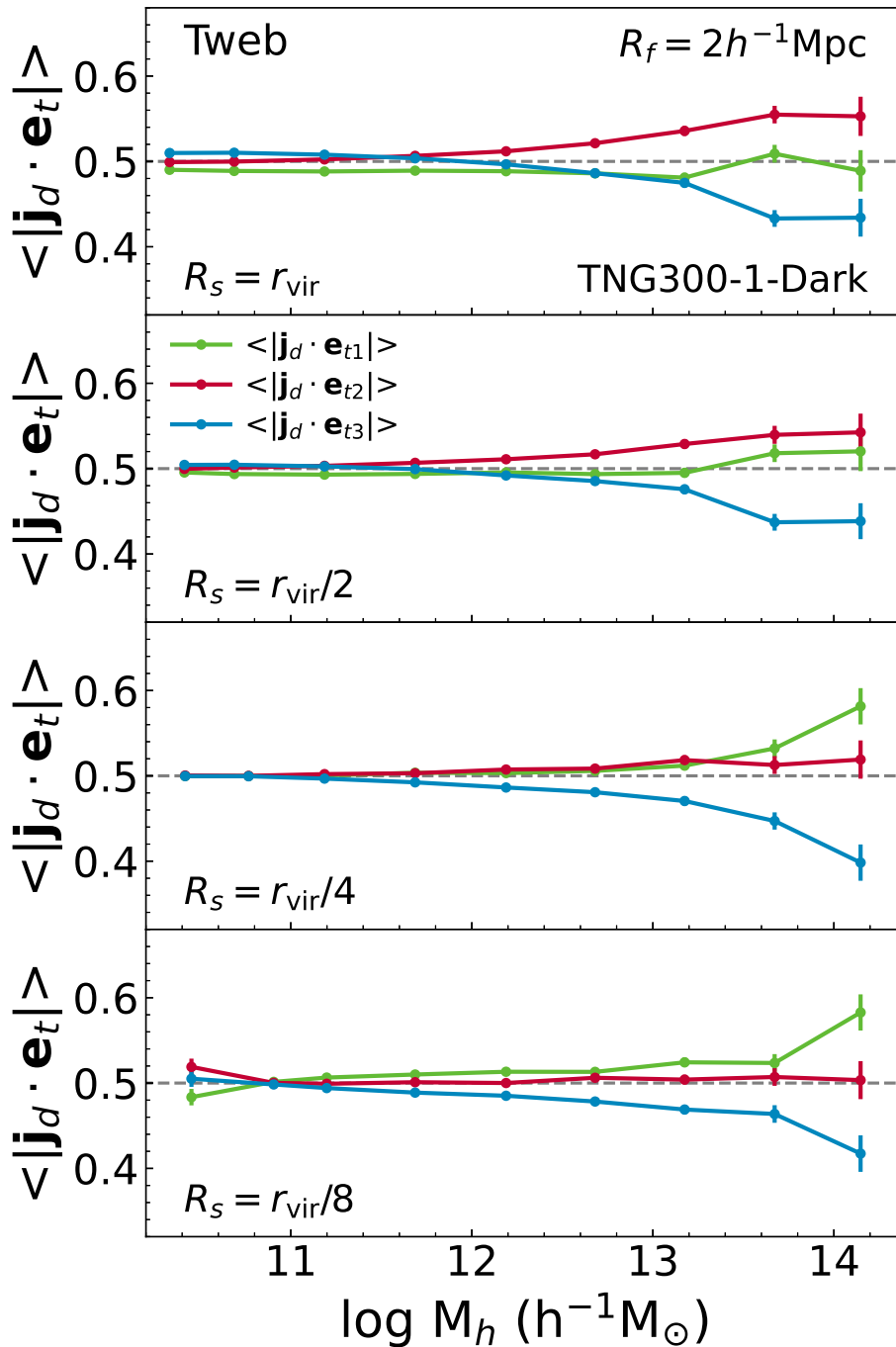


Fig. 2.— Mean absolute values of the cosines of the angles between the halo spin vectors measured at r_{vir} , $r_{\text{vir}}/2$, $r_{\text{vir}}/4$ and $r_{\text{vir}}/8$ (from top to bottom panels, respectively) and three principal axes of the tidal fields smoothed on the scales of $R_f = 2 h^{-1} \text{Mpc}$ as a function of halo mass at $z = 0$ from the TNG300-1-Dark simulation.

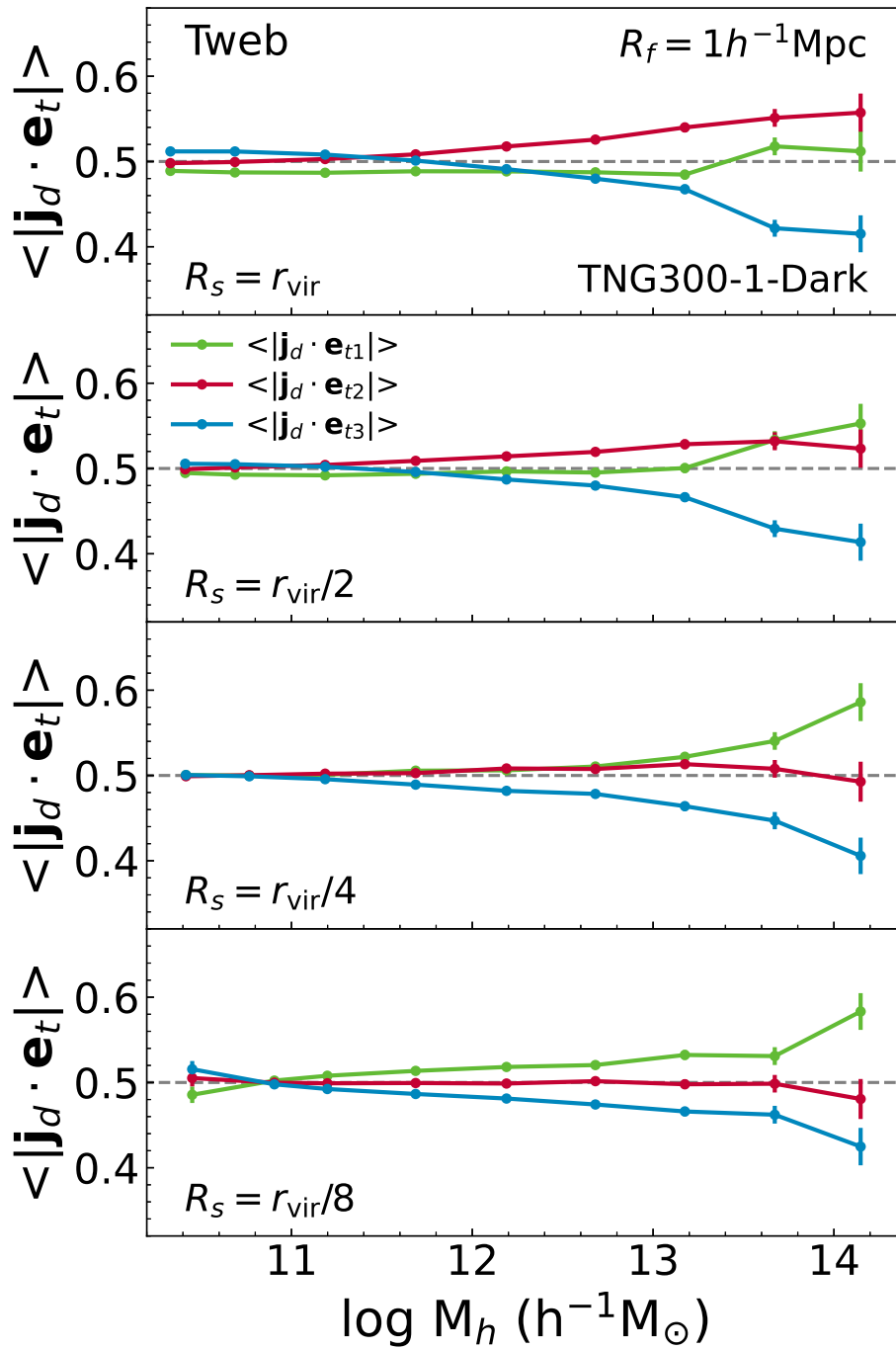


Fig. 3.— Same as Figure 2 but for the case of $R_f = 1 h^{-1} \text{Mpc}$.

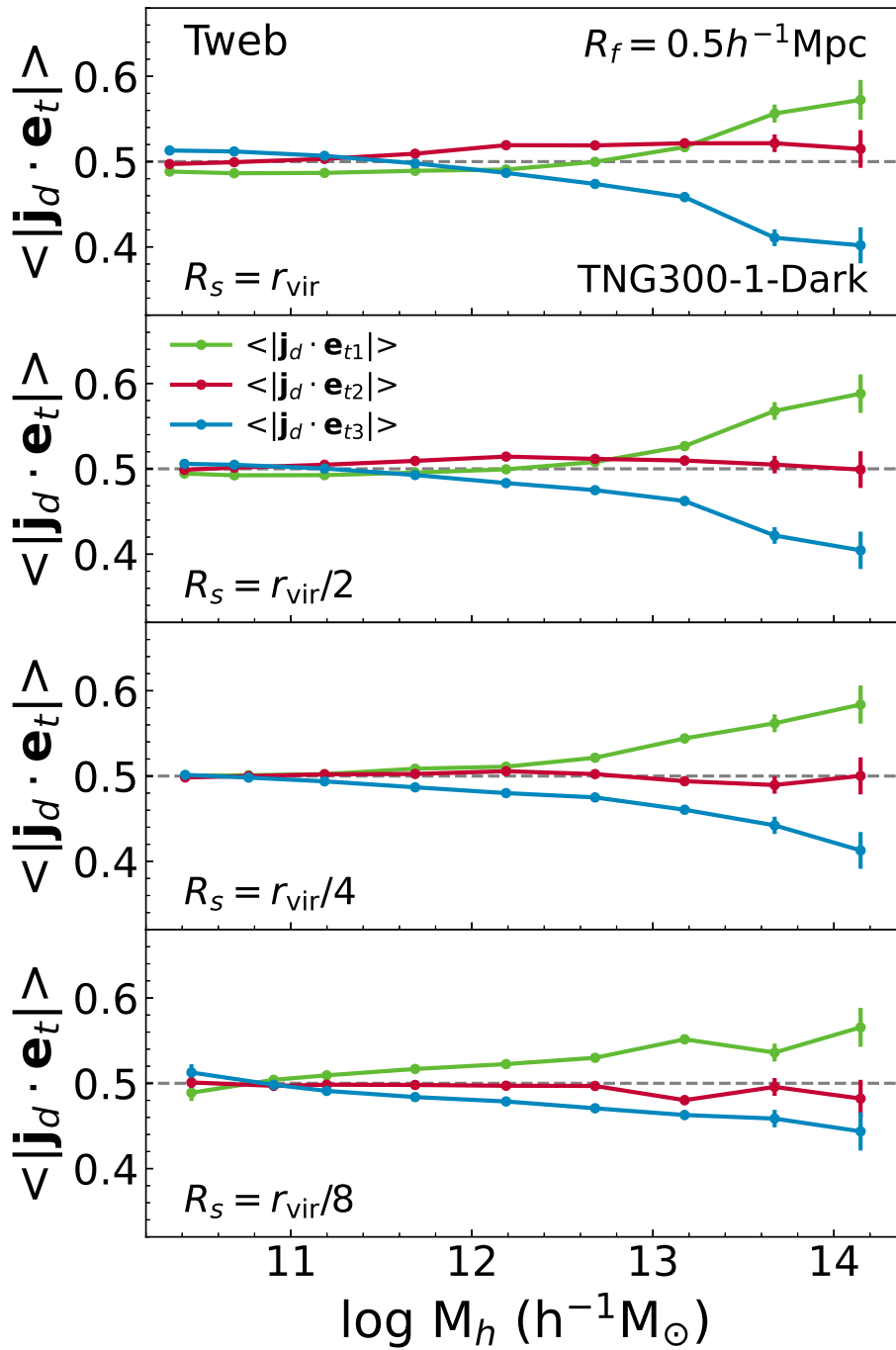


Fig. 4.— Same as Figure 2 but for the case of $R_f = 0.5 h^{-1} \text{Mpc}$.

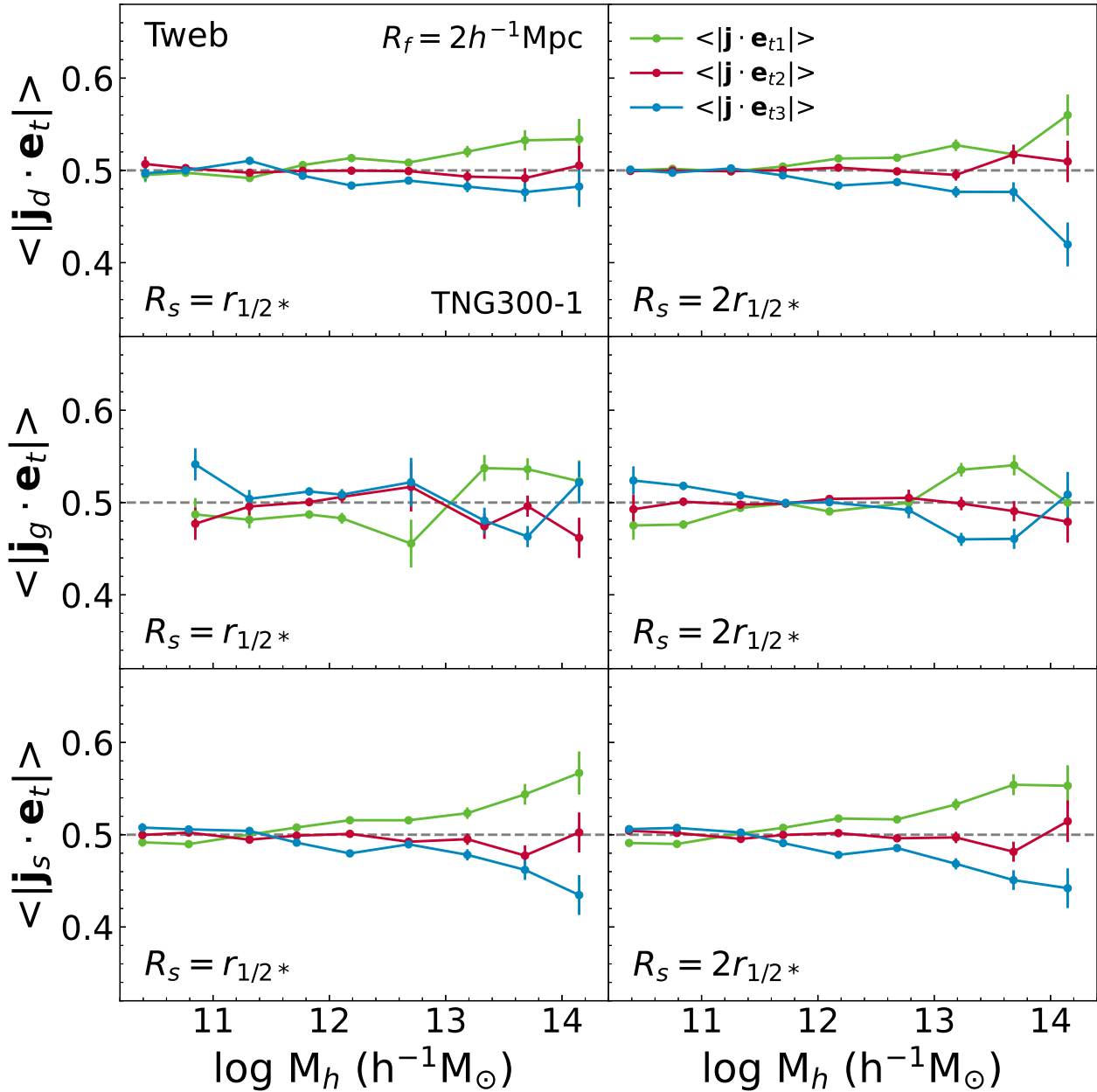


Fig. 5.— Orientations of the spin vectors of the DM (top panels), non-stellar gas (middle panels) and stellar (bottom panels) components measured at $r_{1/2*}$ (left panels) and $2r_{1/2*}$ (right panels) in the Tweb principal frame on the scale of $R_f = 2 h^{-1} \text{Mpc}$ as a function of halo mass at $z = 0$ from the TNG300-1 simulation.

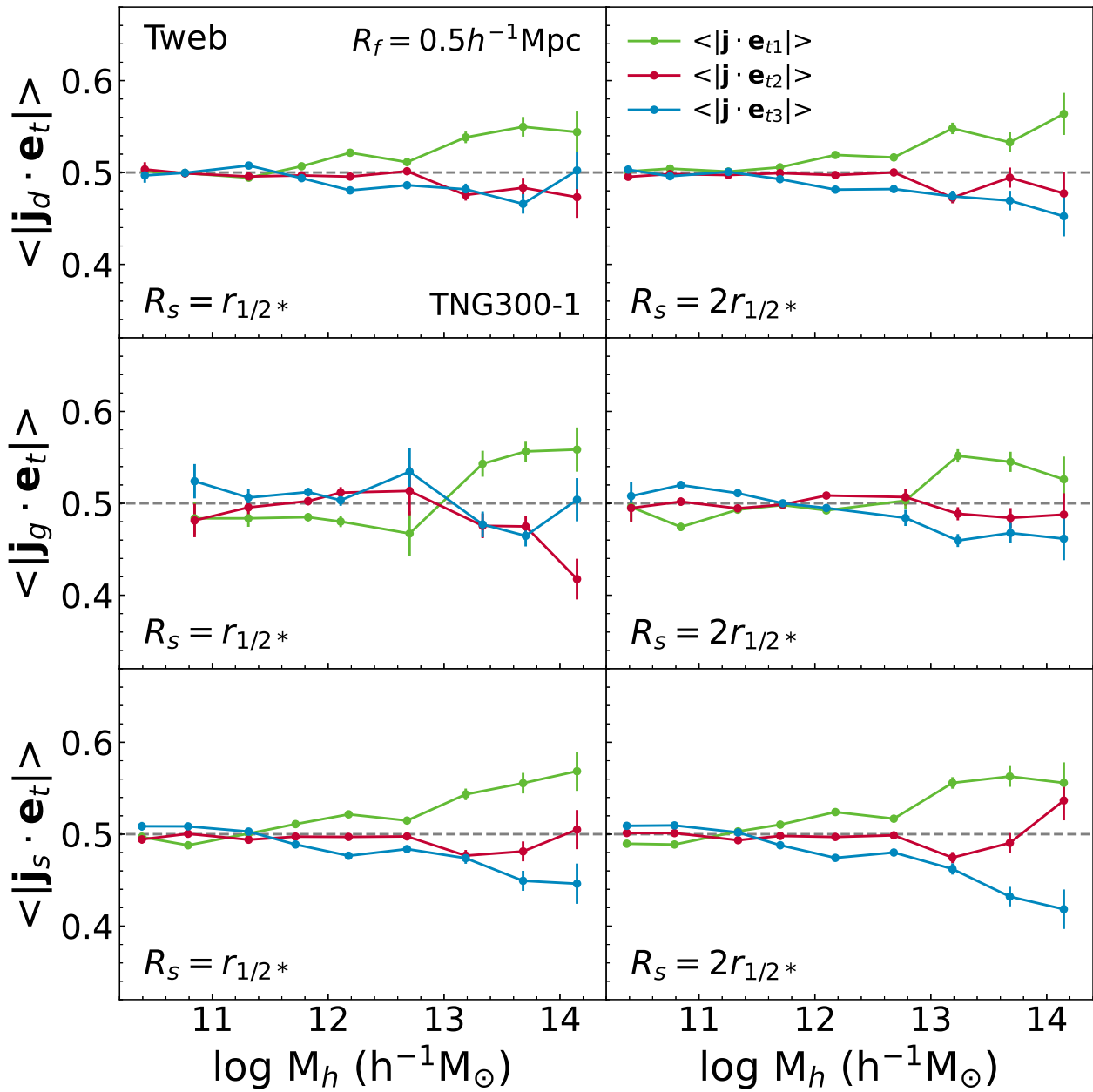


Fig. 6.— Same as Figure 5 but at $R_f = 0.5 h^{-1} \text{Mpc}$.

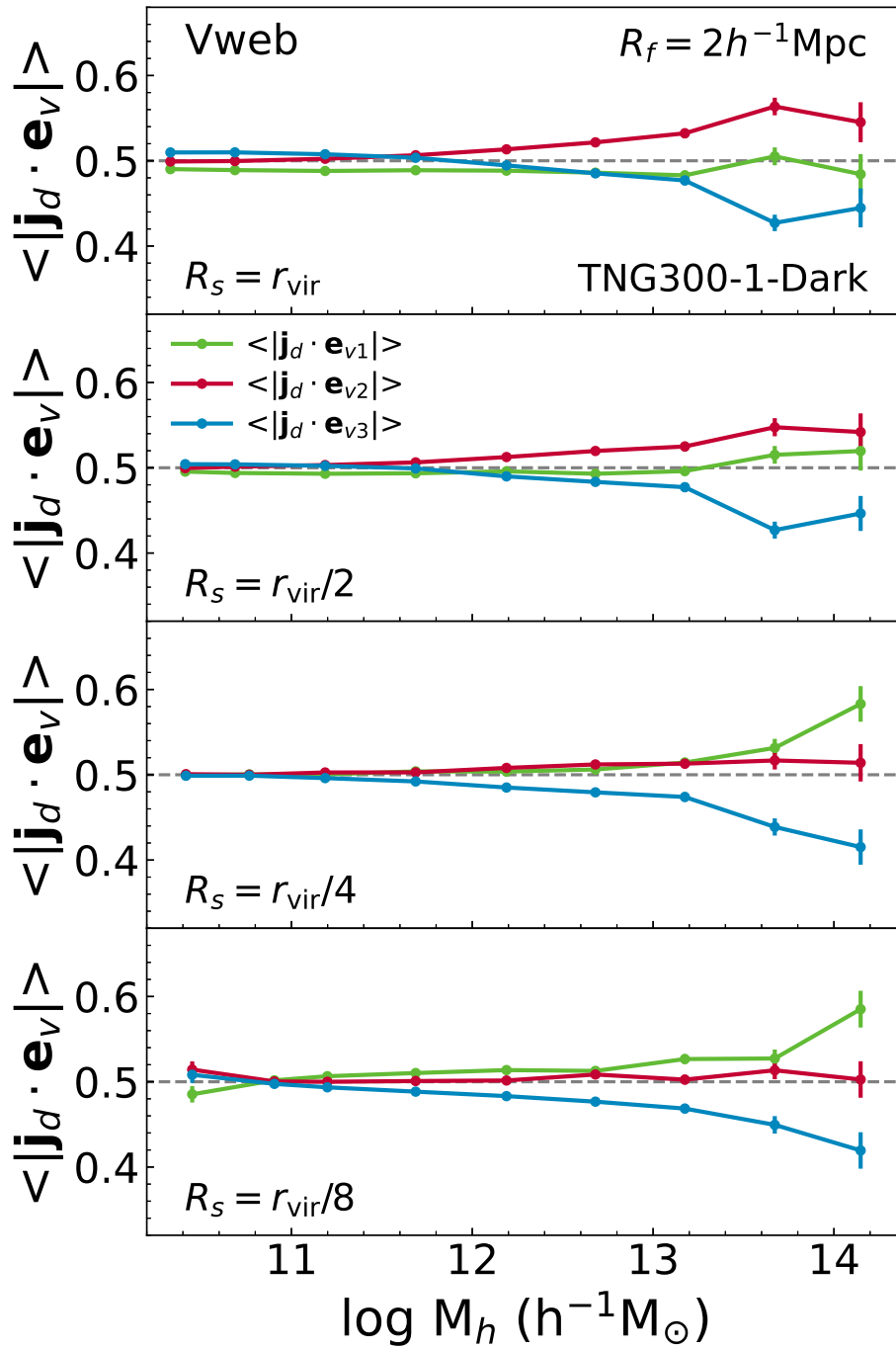


Fig. 7.— Same as Figure 2 but with the Vweb instead of the Tweb.

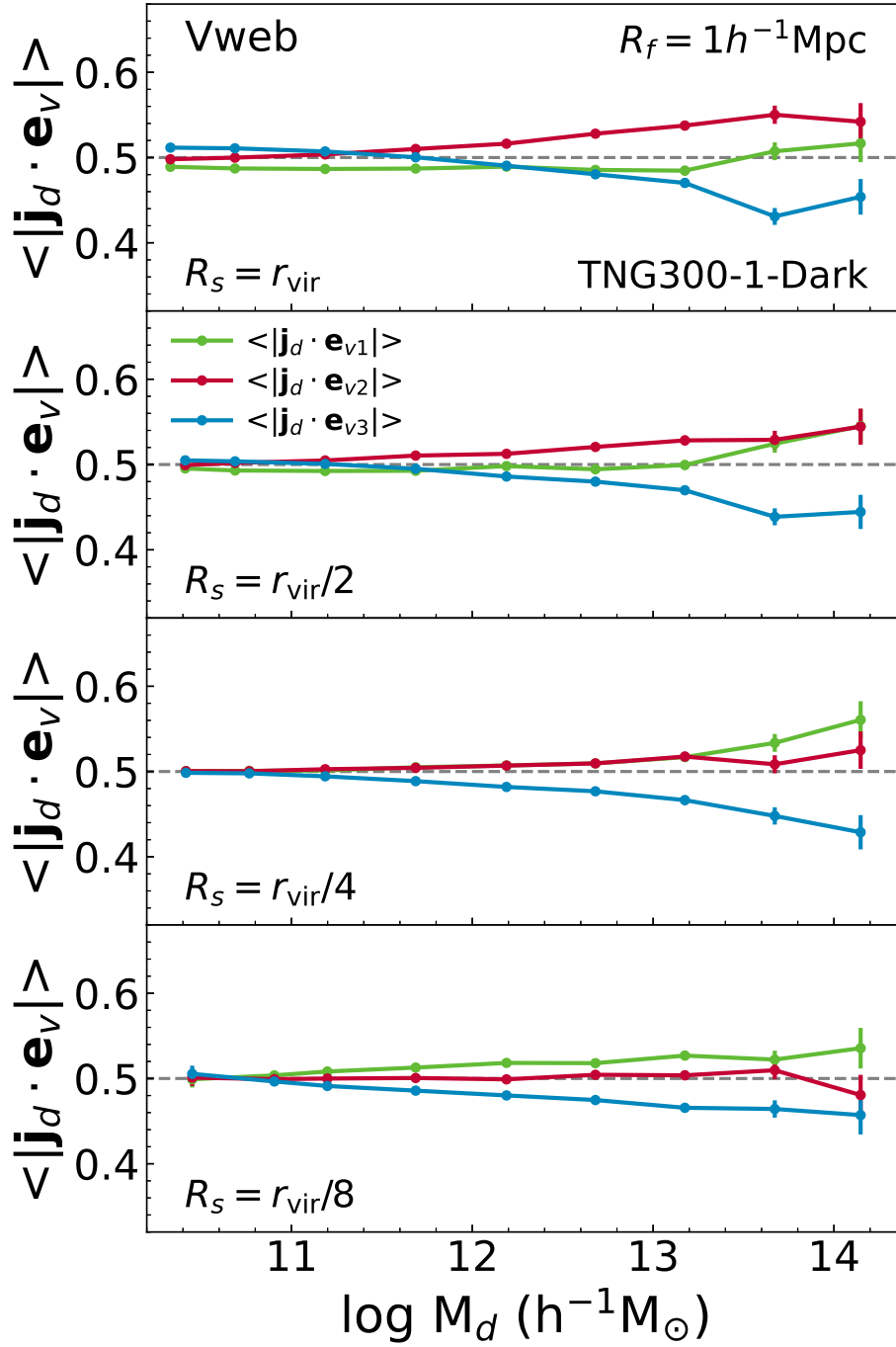


Fig. 8.— Same as Figure 7 for the case of $R_f = 1 h^{-1} \text{Mpc}$.

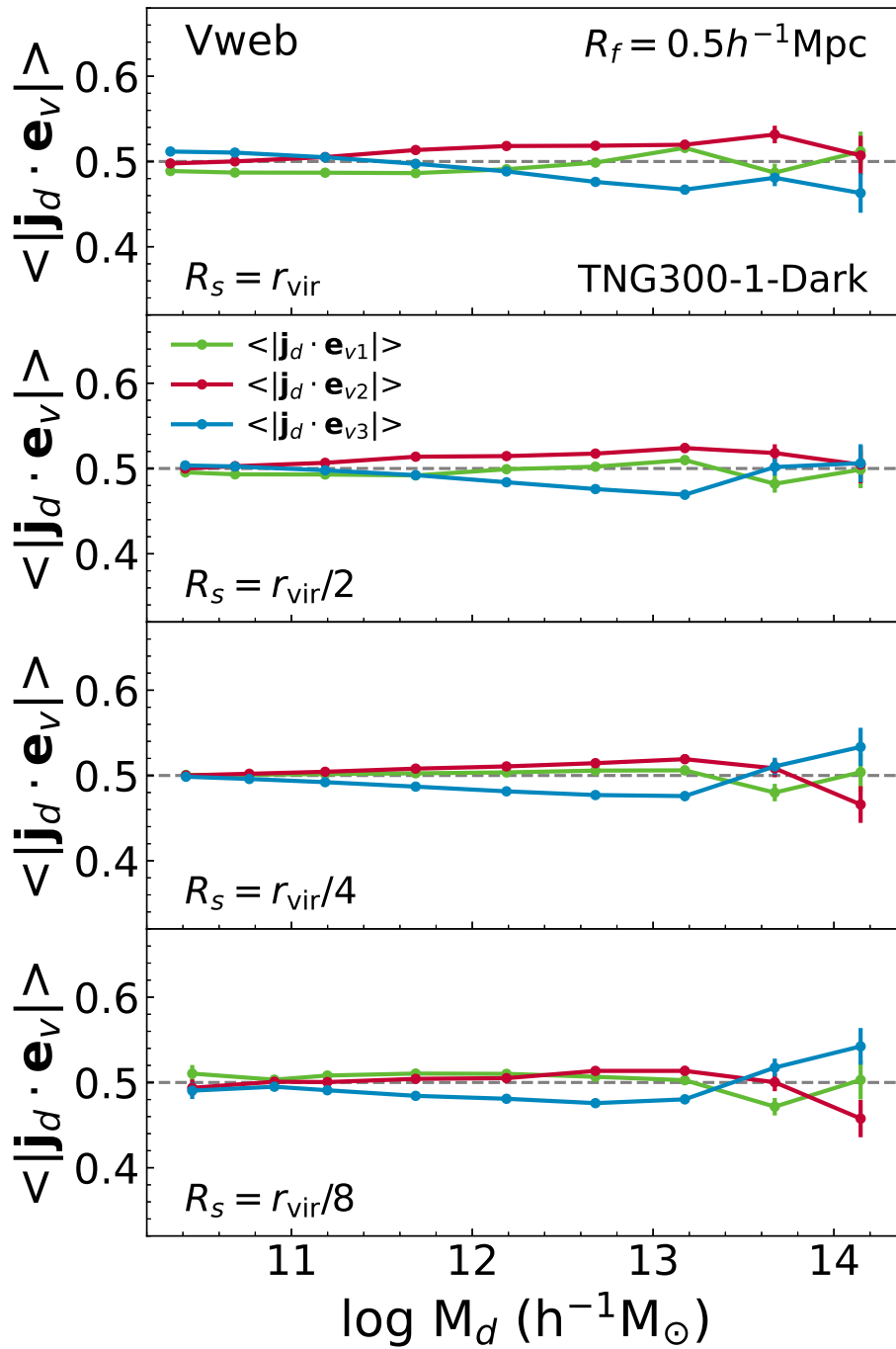


Fig. 9.— Same as Figure 7 for the case of $R_f = 0.5 h^{-1} \text{Mpc}$.

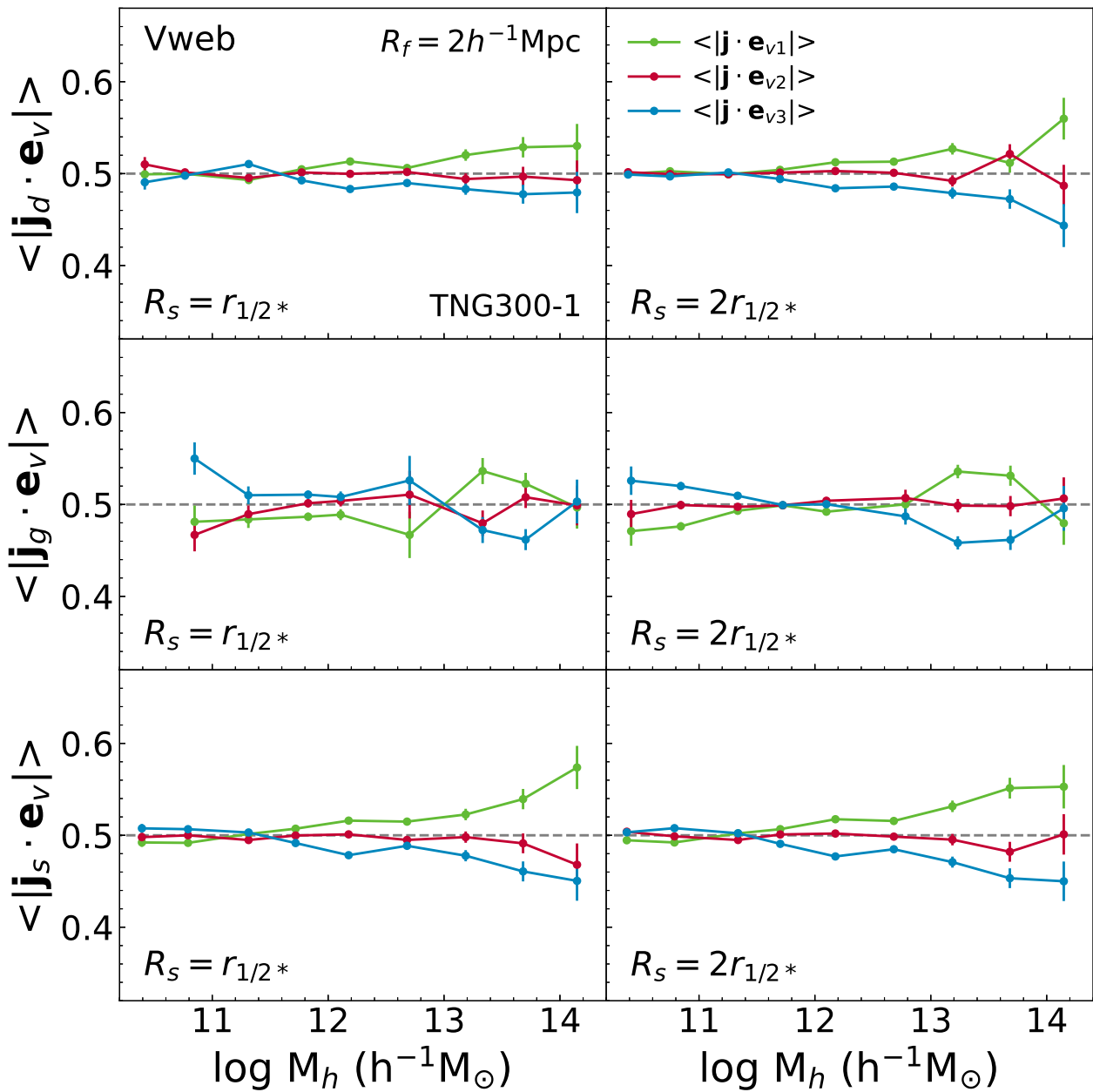


Fig. 10.— Same as Figure 5 but with the Vweb instead of the Tweb.

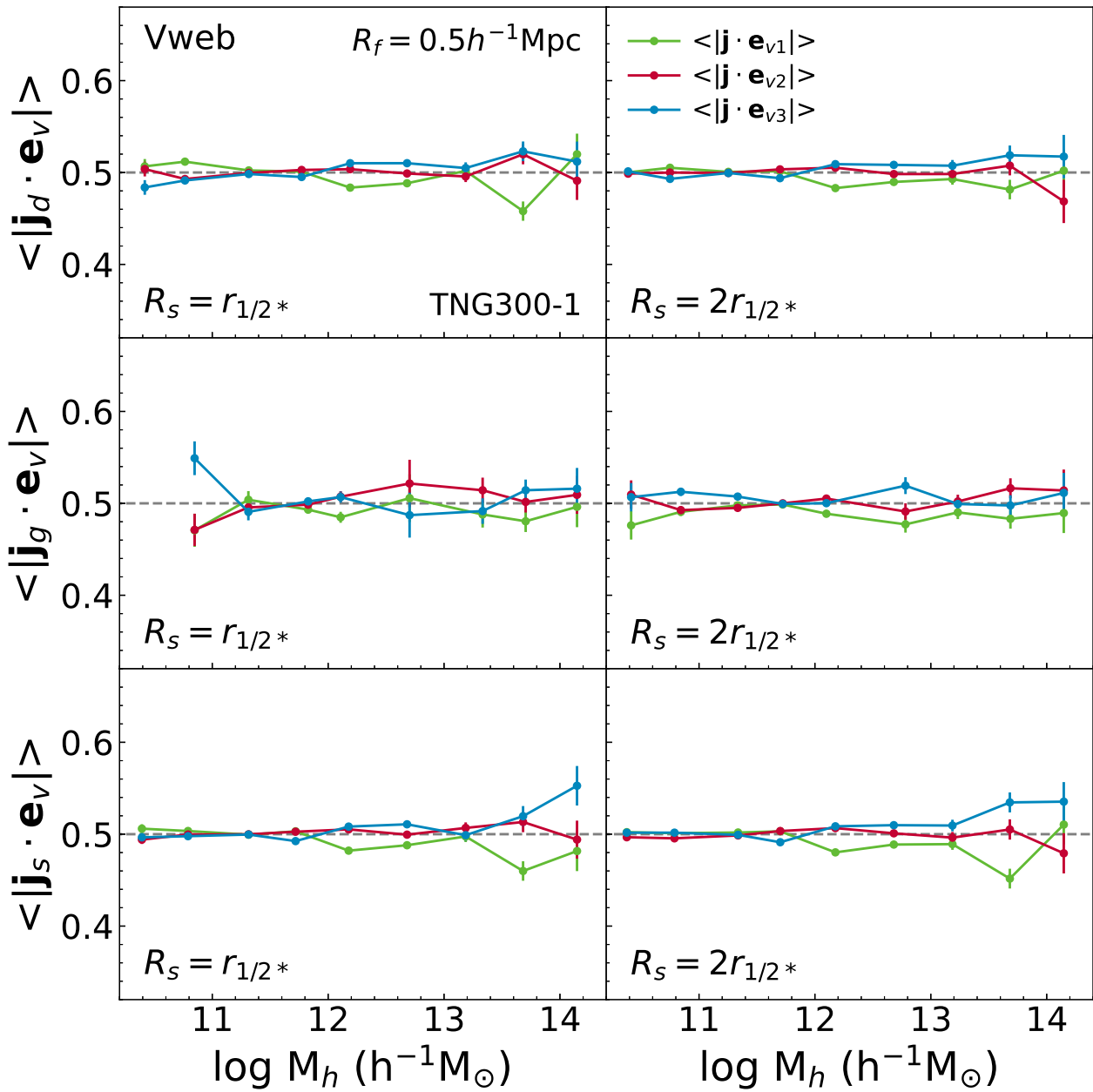


Fig. 11.— Same as Figure 10 for the case of $R_f = 0.5 h^{-1} \text{Mpc}$.

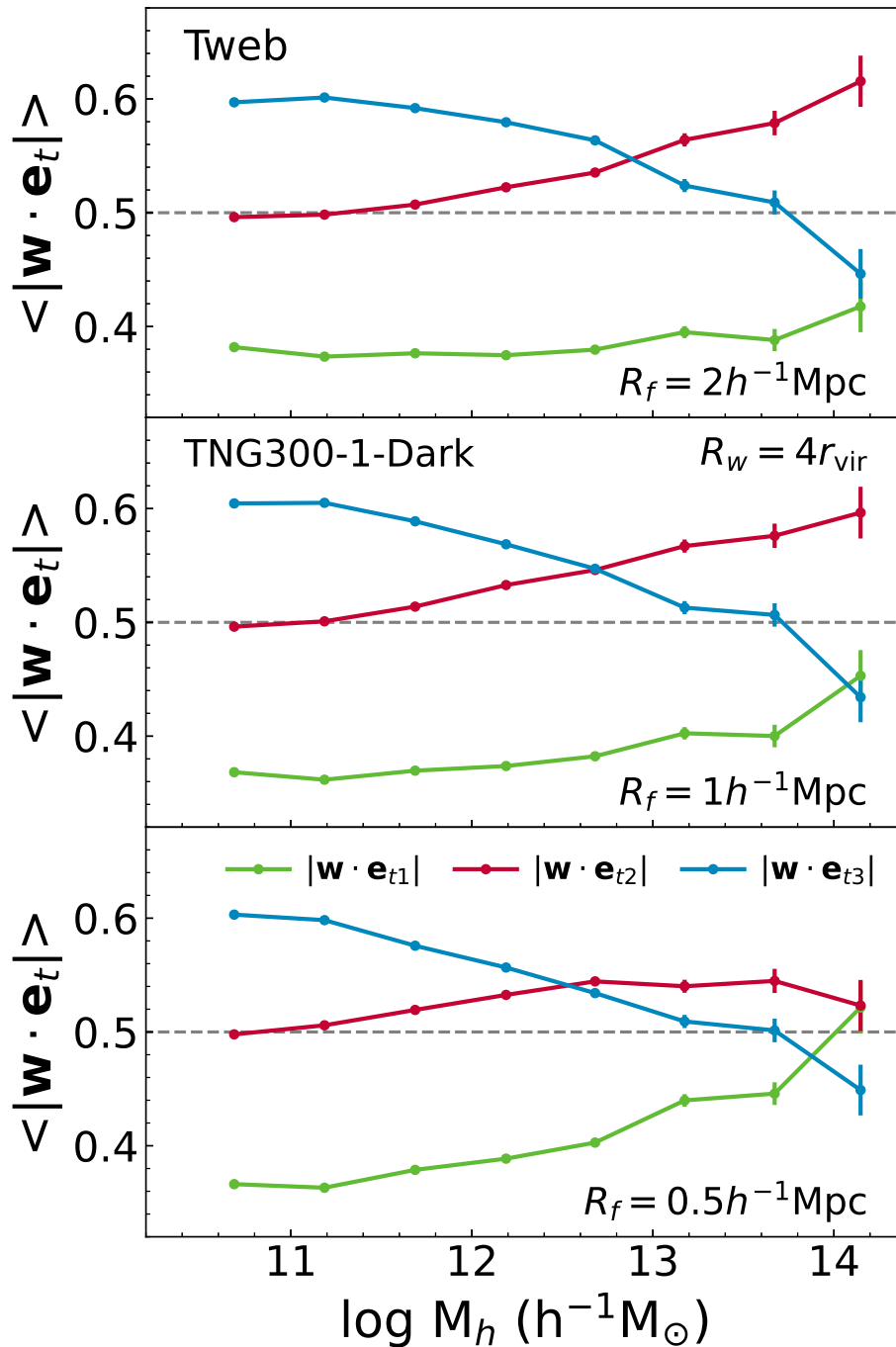


Fig. 12.— Orientations of the vorticity vectors in the Tweb principal frame on three different scales of $R_f = 2, 1$ and $0.5 h^{-1} \text{Mpc}$ (from top to bottom panels, respectively) as a function of halo mass at $z = 0$ from the TNG300-1-Dark simulation.

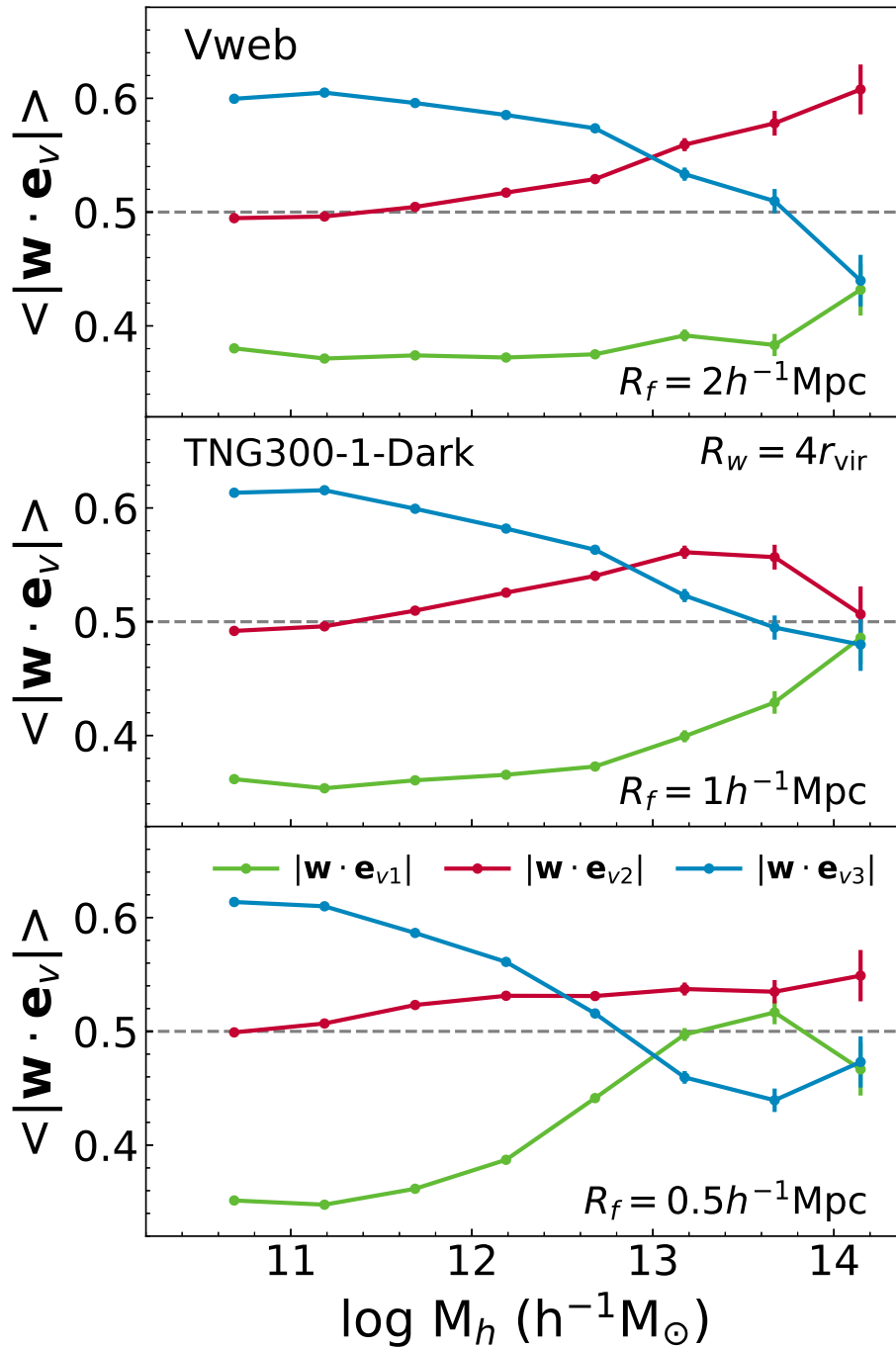


Fig. 13.— Same as Figure 12 but in the Vweb principal frame.

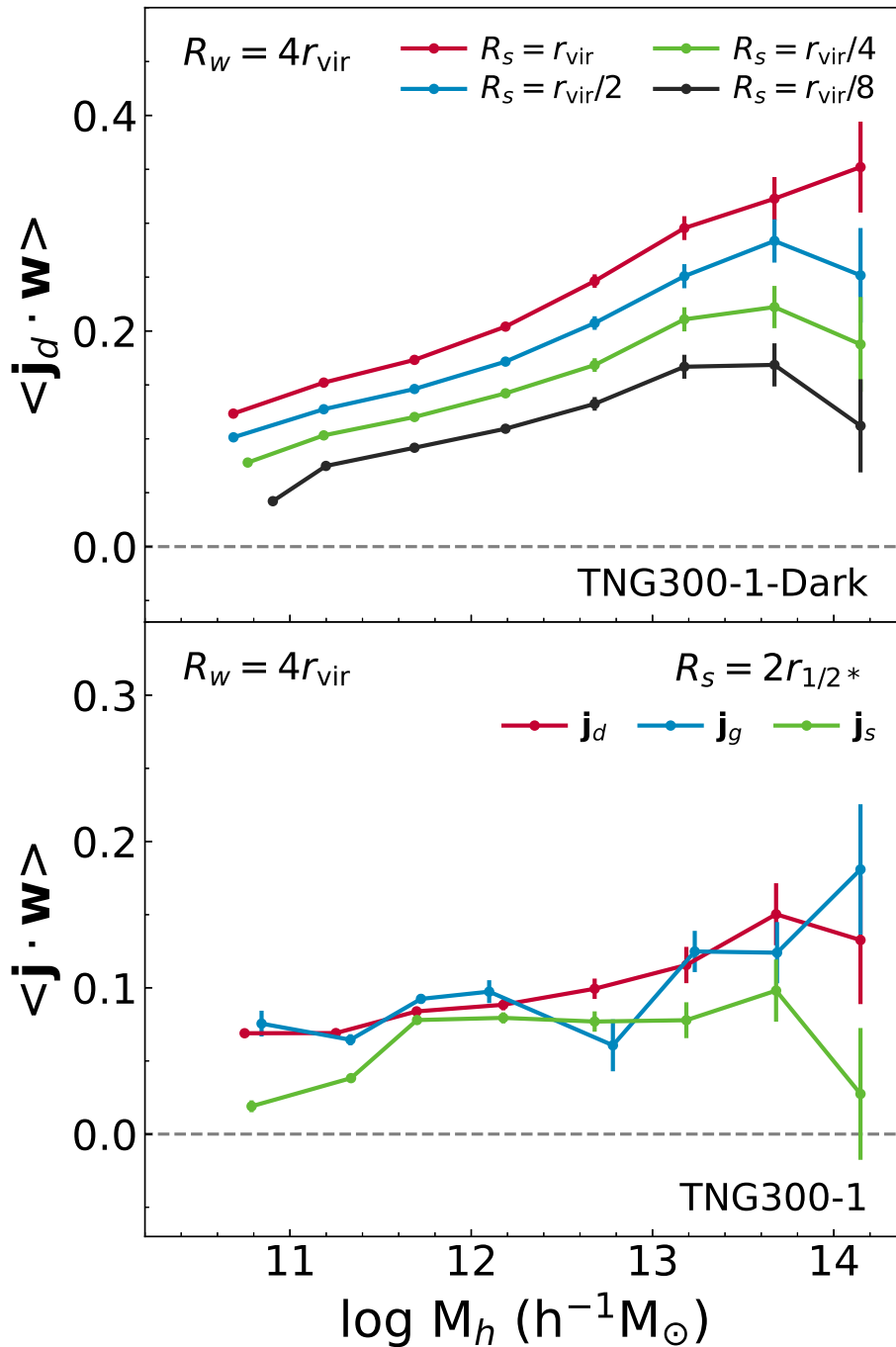


Fig. 14.— Dot products between the halo spin and vorticity vectors as a function of the halo mass: halo spin vectors measured at four different radii from the TNG300-1-Dark simulation (top panel); spin vectors of the DM, gas, and stellar components measured at $2r_{1/2*}$ from the TNG300-1 simulation (bottom panel).

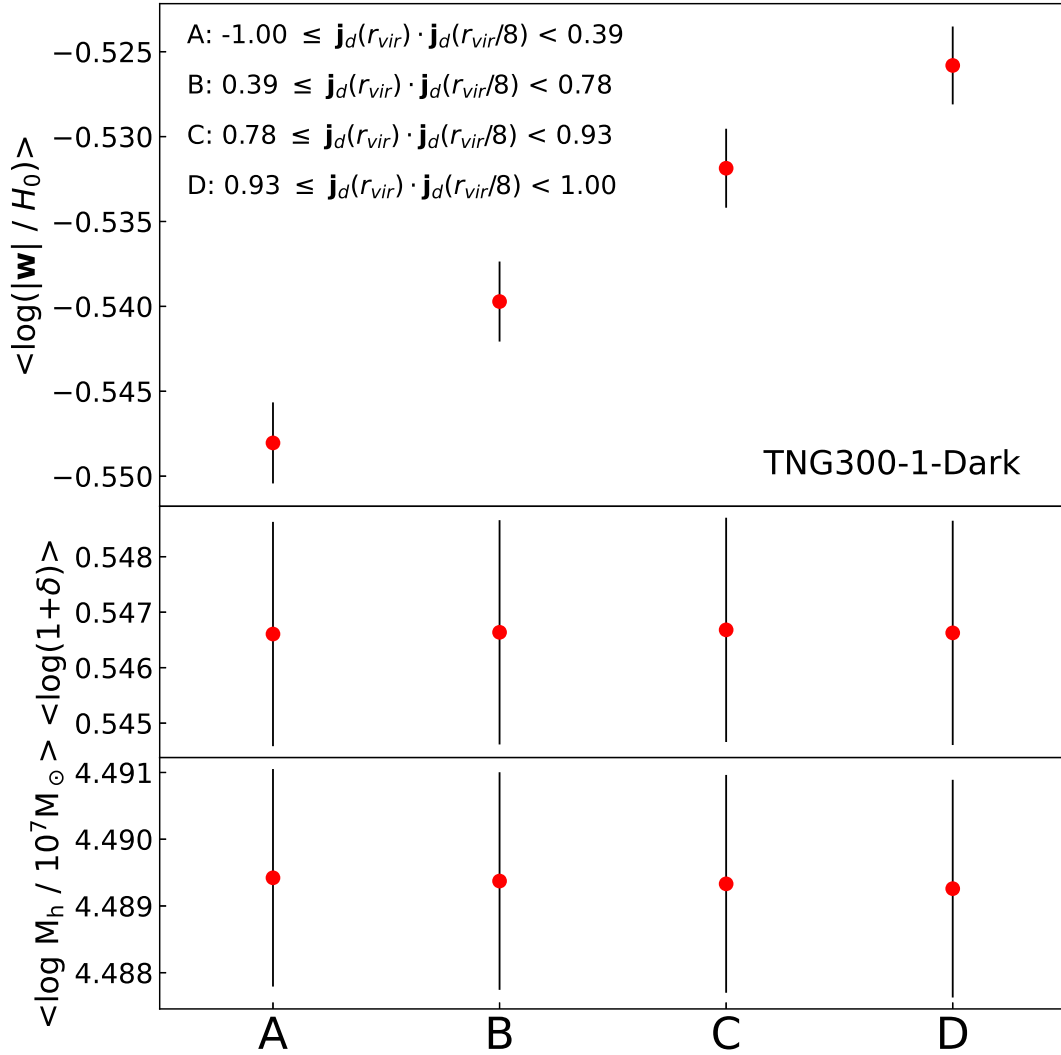


Fig. 15.— Mean values of the logarithms of the vorticity magnitudes (top panel), densities (middle panel), and halo masses (bottom panel) from four controlled samples classified by the dot-products between the halo spin vectors measured at two different radii from the TNG300-1-Dark simulation.

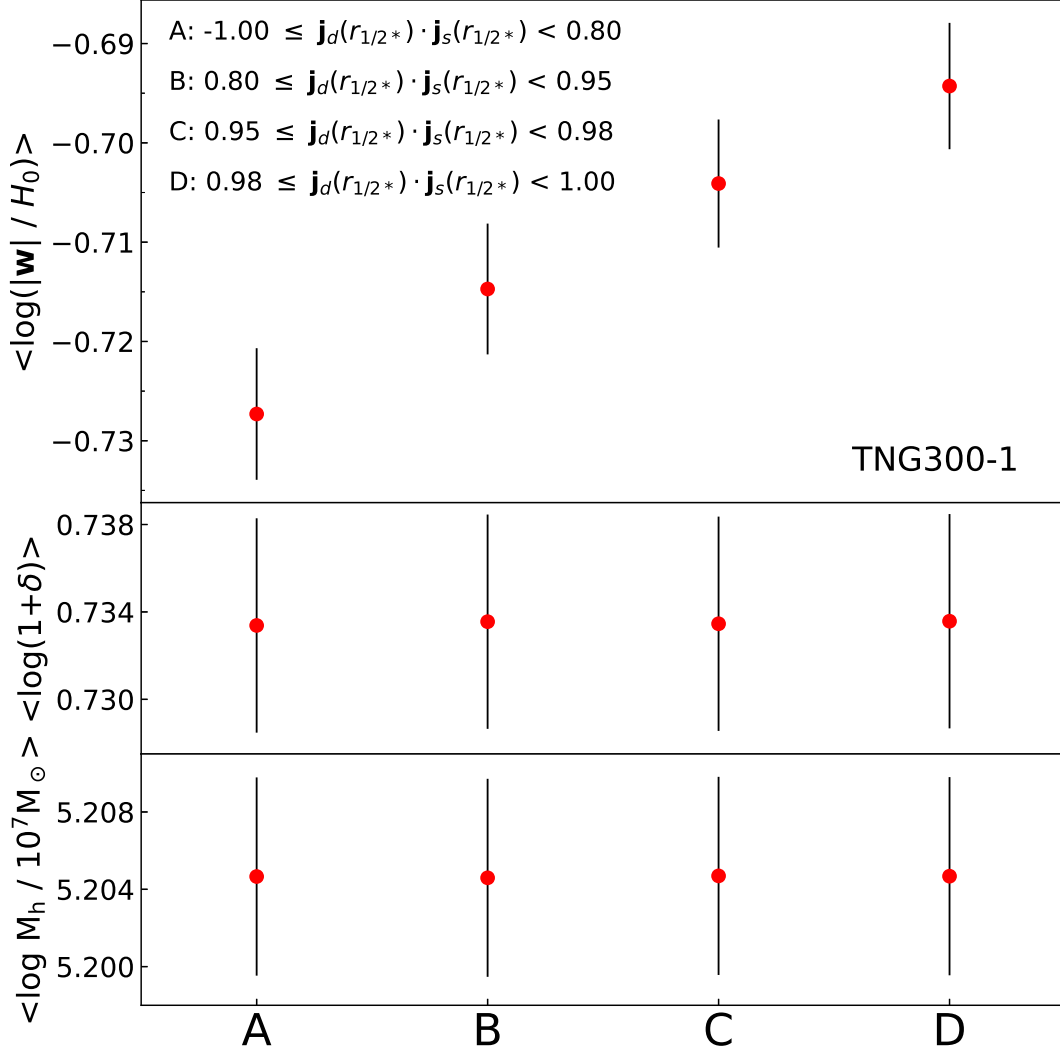


Fig. 16.— Same as Figure 15 but from the controlled samples classified by the dot-products between the DM and stellar spin vectors from the TNG300-1 simulation.

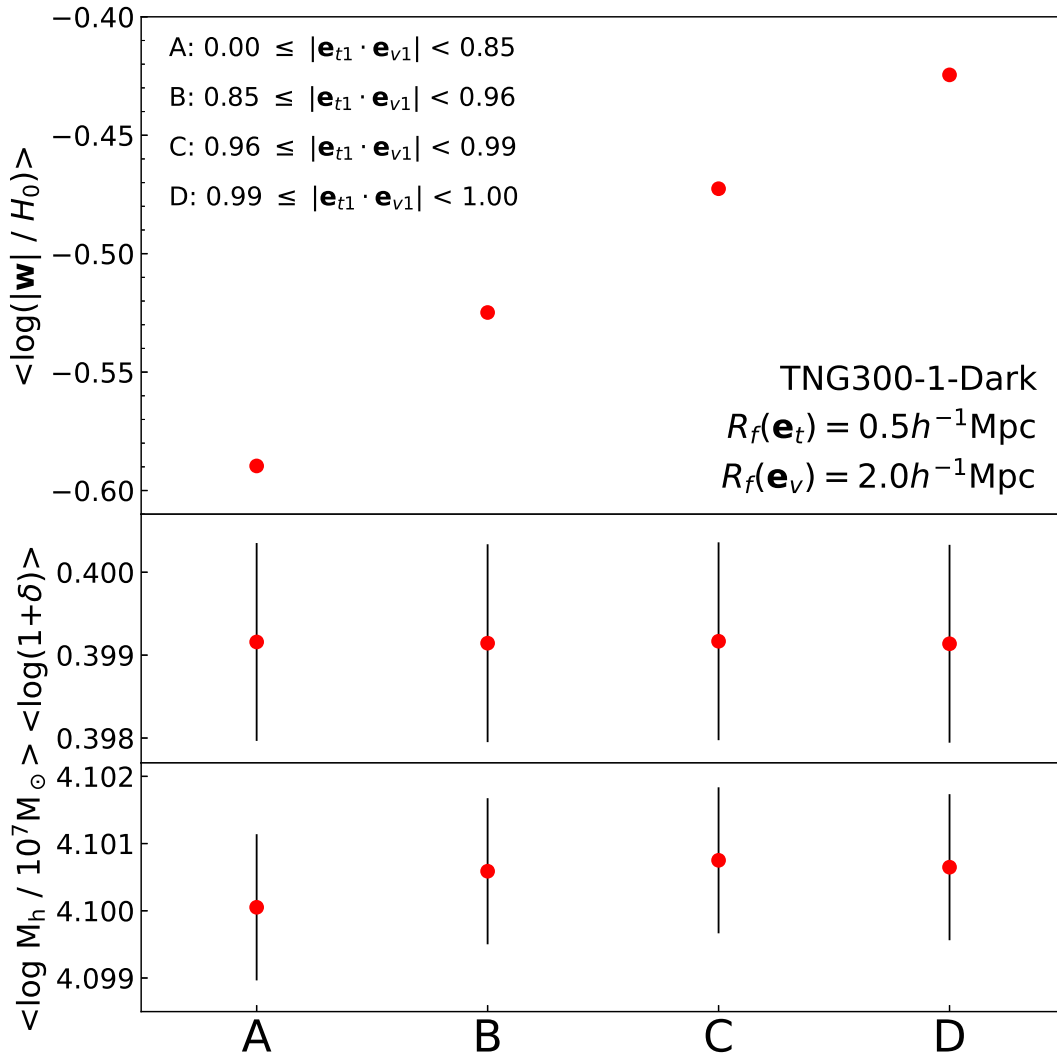


Fig. 17.— Mean values of the logarithms of the vorticity magnitudes (top panel), densities (middle panel), and halo masses (bottom panel) from four controlled samples classified by the absolute values of the dot-products between the Tweb and Vweb major principal axes measured at two different smoothing scales from the TNG300-1-Dark simulation. The errors in the the logarithms of the vorticity magnitudes are invisible due to their small sizes.

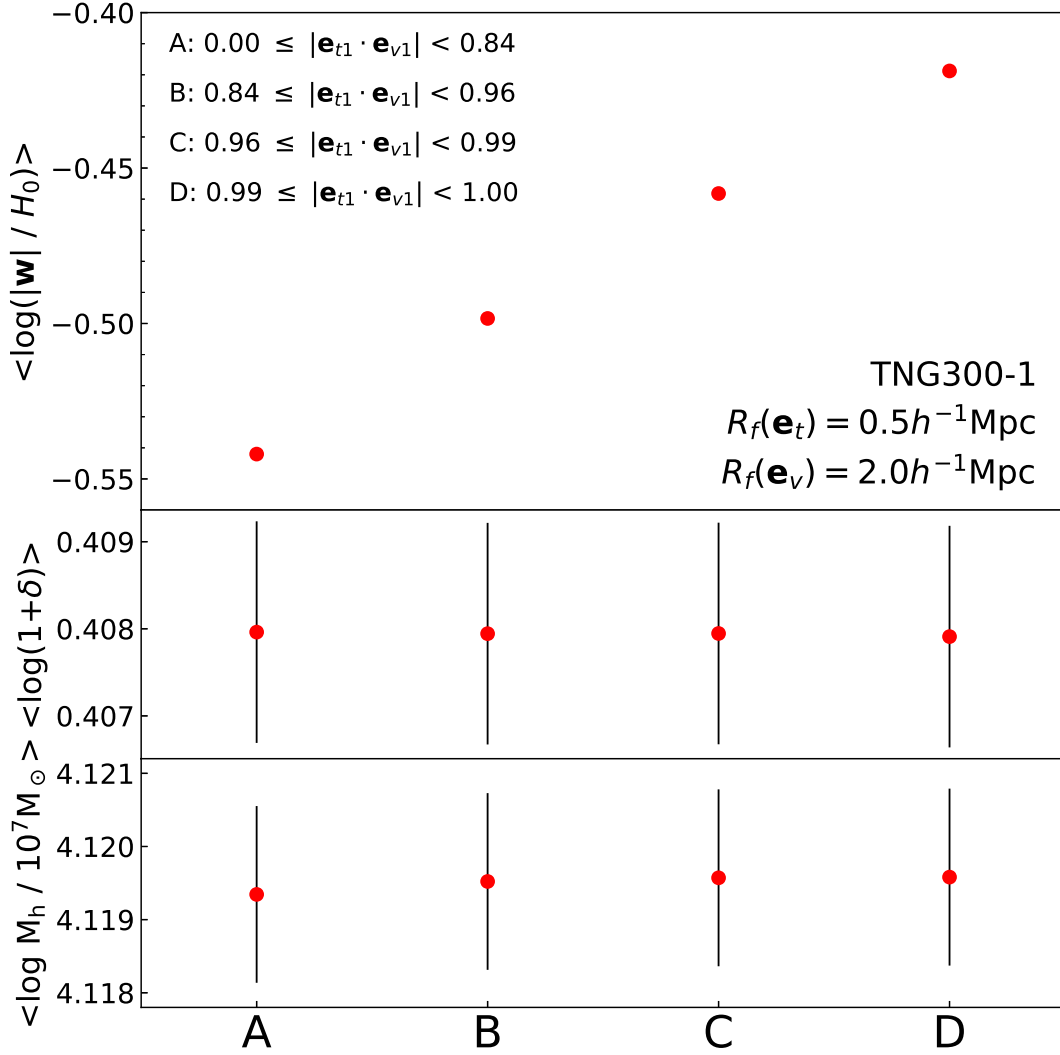


Fig. 18.— Same as Figure 17 from the TNG300-1 simulation.